Photon Migration In Turbid Media:
Time-Resolved Optical Imaging In Tissue-Like Phantom

by

Jun Wu

B.S., Physics
Peking University
(1989)

M.S., Physics
Massachusetts Institute of Technology
(1992)

SUBMITTED TO THE HARVARD-MIT DIVISION OF
HEALTH SCIENCES AND TECHNOLOGY
IN PARTIAL FULFILLMENT OF THE REQUIREMENTS
FOR THE DEGREE OF DOCTOR OF PHILOSOPHY

at the
Massachusetts Institute of Technology
May, 1996
[June 1996]

© 1996 Jun Wu

Signature of Author: _____

Division of Health Sciences and Technology
May 15, 1996

Certified by _____

Michael S. Feld
Professor, Department of Physics
Thesis Supervisor

Accepted by _____

Martha L. Gray, Co-director
Division of Health Sciences and Technology

Photon Migration In Turbid Media:
Time-Resolved Optical Imaging In Tissue-Like Phantom

by

Jun Wu

Submitted to the Harvard-MIT Division of Health Sciences and technology in partial
fulfillment of the requirements for the degree of Doctor of Philosophy

Abstract

Time-resolved photon migration is under extensive study for medical imaging, and there is great interest in developing an optical method for localizing lesions within the body, such as in breast tumor detection. Because biological tissue is highly scattering in the NIR region, the problem is one of imaging objects embedded in a turbid medium. In our approach, we detect early arriving photons (~100 ps) to ensure the optimal trade-off between the S/N and the spatial resolution. In addition, we combine fluorescence spectroscopy with tomographic technique to provide enhanced contrast between the embedded lesions and the surrounding tissue.

Both theoretical and experimental research works are reported in this thesis. Photon migration approach was explored to provide a theoretical understanding of problem of light propagation in tissue. In particular, a convolution method was introduced to model the boundary effects on the time-resolved signal. Experimentally, it was first demonstrated that the long fluorescence lifetime does not obscure the temporal resolution in the early arriving signals because the excitation transition of the fluorophores is almost instantaneous. Then a prototype tomographic imaging system was constructed using the state-of-the-art pico-second laser and streak camera, which provides 10 ps temporal resolution and single photon counting capability. Using phantom samples with typical parameters of human breast, we could detect 1 mm embedded fluorophores within a minute. In addition, we developed a simple, analytical inverse algorithm using the Laplace transformation, which is able to localize embedded fluorophores with an accuracy about 0.3 mm and to resolve multiple fluorophores if they are separated by more than 4-5 mm from each other. The effect of background fluorescence on the information extraction about the embedded objects was also investigated using the phantom samples. With 10:1 contrast ratio, we could localize the embedded 5 mm object with an accuracy of 1.5 mm. Finally, the S/N of the system was fully analyzed, which provides quantitative information about the expected results in the potential clinical applications of detecting breast tumor using fluorescence contrast agents.

Thesis Supervisor: Michael S. Feld, Professor of Physics

Acknowledgments

Table of Contents

List of Figures

List of Tables

Chapter 1

Introduction

1.1 Background: Optical Imaging, Tissue Turbidity and Photon Migration

The application of basic physics and advanced technologies to biomedical research has had a tremendous impact on clinical diagnostics. Various imaging modalities, such as computed tomography (CT) and magnetic resonance imaging (MRI), have become standard diagnostic tools in clinical medicine in the past decades. These techniques have allowed physicians to obtain information about internal structures and embedded lesions non-invasively.

The use of lasers and optical detection for biomedical imaging has become a fast-growing area of research of great current interest [Chance & Alfano, 1995; Alfano & Fujimoto, 1996] because it offers several advantages. (1) In the near infrared (NIR) wavelength range, the absorption of light by biological tissues is very small. For example, the absorption coefficient, μ_a, of biological tissue is on the order of 0.001-0.01 mm^{-1}. In other words, photons are absorbed by tissue, on average, after 100-1000 mm travel distance inside biological tissue [Yodh & Chance, 1995]. As a result, NIR light can easily penetrate deeply into the tissue, and the transmitted and/or retroreflected light bears clues about tissue it has passed. In addition, the small absorption allows NIR light to be well tolerated in large doses without generating a "cooking" effect, since only a small portion of this energy is absorbed by the tissue and converted to heat. (2) Unlike

1

ultraviolet (UV) light, the energy of the NIR photons is generally small compared to that required to break chemical bonds. Therefore, it can be safely used in clinical diagnosis without great concern for any ionizing or mutagenic effects. (3) The combination of imaging with spectroscopic techniques in principle can provide physicians with an objective assessment of the biological tissue based on quantitative biochemical and/or morphological information highly specific to disease progression. For example, NIR absorption spectroscopy has been routinely used to monitor tissue oxygenation status in clinical settings [Weinberger & Drazen, 1994]. NIR Raman spectroscopy has been explored to detect atherosclerosis [Baraga, 1992; Brennan, 1995]. Fluorescence spectroscopy is useful in characterizing various diseases such as atherosclerosis and dysplasia [Richards-Kortum, 1990]. Fluorescence microscopy using contrast agents has been a standard research tool in studying various physiological/pathophysiological conditions [Tsien & Waggoner, 1995].

However, a key fundamental problem has to be addressed before optical imaging can realize its goals in clinical applications. Unlike X-rays, NIR photons are strongly scattered by biological tissues. For example, the scattering coefficient, μ_s, of biological tissue is typically on the order of 10 mm^{-1}. In other words, photons are scattered by tissue, on average, 10 times per 1 mm traveling distance. The chief contributor to the scattering of tissues is their organelle content, such as mitochondria and nuclei [Chance, 1995]. The microscopic refractive-index mismatch between the inside and the outside of these small objects leads to the change of direction in which the photons travel. Because their sizes (~ 1 μm) are similar to the NIR wavelength, they are very good scatterers

2

compared with particles of other sizes, such as whole cells (~ 10 μm). It is the average effects of these ultrastructures that yield the macroscopic optical properties of tissues. Multiple scattering can severely degrade the image resolution by randomizing the photon paths traversing the media. This has been the major hurdle to prevent optical imaging from being used clinically. In order to overcome the tissue turbidity, intensive research studies [Chance & Alfano, 1995; Alfano & Fujimoto, 1996] have emerged in the last decade (1) to provide a better understanding of the underlying physics problem, i.e., photon migration in turbid media, and (2) to explore experimental approaches, most of which use time-resolved techniques, varying from time domain measurements to frequency domain to coherent methods, to reveal a maximum amount of spatial information about the internal structures.

This thesis reports theoretical and experimental research in this field. The photon migration picture is studied to provide a theoretical understanding of the problems of light propagation in tissue, especially the boundary condition effects on time-resolved optical detection (Chapter 2). Experimentally, ultrafast time-resolved tomography is explored as a potential tool for biomedical diagnostic imaging (Chapters 3 and 4). For convenience, relevant research by other groups is reviewed separately in the corresponding sections of this thesis. However, it should be emphasized that the two aspects of the research are inherently interconnected and have a common ultimate goal of providing optical diagnostic/imaging tools for clinical use.

1.2 Potential Applications: Breast Cancer And Mammography

Several target clinical applications have been suggested in the research of optical imaging [Chance, 1995]. These include detection of brain hematomas and tumors, breast tumors, prostate tumors and monitoring of tissue oxygenation, metabolic and/or functional states, etc. Among these, breast tumor detection has attracted the most attention [Chance & Alfano, 1995; Alfano & Fujimoto, 1996].

Breast cancer is both one of the most common and one of the most treatable of all human malignancies. It is the leading cause of death among American women who are 40 to 55 years of age. In the United States, one out of eight women will develop breast cancer in her lifetime, and one out of thirty will die of breast cancer, i.e., more than 40,000 deaths per year [Henderson, 1994]. Fortunately, breast cancer is one of the few tumors for which there is conclusive evidence that early diagnosis will substantially decrease mortality. Five major studies indicate that "annual screening of all women 40 years of age or older by means of state-of-the-art X-ray mammography with two views per breast and physical examination could reduce breast cancer mortality by at least 40% and possibly by as much as 50%" [Marchant, 1994].

However, in the current clinical practice of X-ray mammography, there is a high misdiagnosis rate in identifying and localizing the tumors, especially at their early stages. This is mainly because of the small, non-specific contrast between the tumor mass and the surrounding tissue detected by X-rays, and wide variation in the tissue density of normal breast. (1) False-negative results occur even in the best screening centers. The incidence of such results may reach 10% and, in some mammography centers, may approach 25%

to 30% [Marchant, 1994]. (2) False-positive results may lead to unnecessary biopsy and/or surgery procedures. For each patient diagnosed with breast cancer, another 5 to 10 women are biopsied for suspicious mammography findings [Henderson, 1994]. (3) Current technology can readily detect a 1 cm tumor mass, but smaller tumors present difficulties. However, cancer metastases presumably occur with greatest frequency when the tumor increases from 10^6 cells to 10^9 cells, i.e., from 1 mm to 1 cm in size. It is such metastases that lead to patient deaths, despite excellent local control of their disease [Henderson, 1994]. It is expected that early detection of smaller tumors will increase the survival of these patients. Therefore there is a tremendous need for new technologies to improve breast cancer screening, with higher sensitivity, higher specificity, and better detection of millimeter tumors.

Optical imaging has been identified as a promising technology to improve breast tumor screening. (1) There are many biological features specific to tumors, including increased vasculature, relative deoxygenate state, increased metabolic rate, unique tumor antigens, etc. [Chance, 1995]. These features can be spectroscopically characterized using either intrinsic tissue components [Alfano et al, 1989] or tumor-specific exogenous contrast agents, such as photodynamic therapy (PDT) agents [Johansson, 1993] and fluorescence-labeled antibodies against tumor-specific antigens [Abbas et al, 1994]. (2) The size of the human breast makes it an ideal organ for optical imaging; for a 10 cm breast, a significant amount of NIR light can be transmitted for optical detection. (3) Most importantly, recent research studies have shown the potential of accurate localization of embedded objects in turbid media by time-resolved optical tomography [Chance &

Alfano, 1995; Alfano & Fujimoto, 1996]. The ultimate goal of optical mammography is to produce optimal images with high spatial resolution and good contrast separation.

1.3 Thesis Structure

The overall objective of this thesis research is to develop a photon migration imaging technique to obtain information about objects embedded in turbid media, such as for breast tumor screening. The photon migration picture defines a basic theoretical approach to modeling light propagation in turbid media. Because of its importance, the entire Chapter Two of this thesis is devoted to the discussions of the photon migration picture, including background information and a review of current research approaches and their biomedical applications. In particular, we explore its application to modeling boundary condition effects, which has a big impact on the inverse algorithm used in the time-resolved tomographic imaging experiments presented later in this thesis. Chapters Three and Four describe the experimental aspects of this thesis research, including detailed background information of research by other groups, rationales of using early arriving photons for resolution and fluorescence for contrast in our approach, as well as the phantom experimental results. In Chapter Three, the initial experiments using early arriving fluorescence to detect embedded objects are presented. In particular, we demonstrate that the long fluorescence lifetime does not obscure the temporal resolution, thus good spatial resolution can be achieved. This approach is then advanced in Chapter Four, which describes a prototype tomographic system consisting of a state-of-the-art laser system and streak camera. Phantom experiments using typical human breast

parameters are performed. In addition, a Laplace transform-based inverse algorithm is developed to analyze the multichannel time-resolved data. The phantom results clearly demonstrate the potential of this technique in clinical applications. Lastly, in Chapter Five the accomplishments of this thesis research are summarized and some future directions are discussed.

References

A. Abbas, A. Litchman, & J. Pober, 1994, Cellular and Molecular Immunology, 2nd ed., (W.B.Saunders Company, Philadelphia).

R. Alfano, A. Pradham, G. Tang, & S. Wahl, 1989, "Optical spectroscopic diagnosis of cancer and normal breast tissue," J. Opt. Soc. Am. B, pp 1015.

R. Alfano & J. Fujimoto, 1996, *Advances in Optical Imaging and Photon Migration TOPS-96*, (OSA, Orlando).

J. Baraga, 1992, *In Situ Chemical Analysis of Biological Tissue: Vibrational Raman Spectroscopy of Human Atherosclerosis*, Ph.D. thesis, MIT, Cambridge, MA 02139.

J. Brennan, 1995, *Near IR-Raman Spectroscopy for Human Artery Histopathology*, Ph.D. thesis, MIT, Cambridge, MA 02139.

B. Chance, 1995, "Time-resolved spectroscopy and imaging," SPIE 2389, pp 122.

B. Chance & R. Alfano, 1995, *Proceedings of Optical Tomography, Photon Migration, and Spectroscopy of Tissue and Model Media: Theory, Human Studies, and Instrumentation*, SPIE 2389.

C. Henderson, 1994, Harrison's Principles of Internal Medicine, 13th ed., Chapter 319, (McGraw-Hill, Inc., New York).

J. Johansson, 1993, *Fluorescence Spectroscopy for Medical and Environmental Diagnostics*, Ph.D. thesis, Lund Institute of Technology, Lund, Sweden.

D. Marchant, 1994, Danforth's Obstetrics and Gynecology, 7th ed., Chapter 38, (JB Lippinott Company, Philadelphia).

R. Richards-Kortum, 1990, *Fluorescence Spectroscopy as a Technique for Diagnosis of Pathologic Conditions in Human Arterial, Urinary Bladder, and Gastro-Intestinal Tissues*, Ph.D. thesis, MIT, Cambridge, MA 02139.

R. Tsien & A. Waggoner, 1995, Handbook of Biological Confocal Microscopy, 2nd ed., Chapter 16, (Plenum Press, New York).

S. Weinberger & J. Drazen, 1994, <u>Harrison's Principles of Internal Medicine</u>, 13th ed., Chapter 214, (McGraw-Hill, Inc., New York).

A. Yodh & B. Chance, March, 1995, "Spectroscopy and imaging with diffusing light," Physics Today, pp 34.

Chapter 2

Photon Migration and Its Applications

The overall objective of this thesis research is to develop a photon migration imaging technique to obtain spatial information about small inhomogeneities embedded in turbid media, such as for breast tumor screening. As mentioned earlier, the photon migration picture defines a basic theoretical approach to modeling the light propagation in turbid media. The understanding of this fundamental physical problem is essential in developing inverse algorithms for optical tomography. In addition, the diagrammatic approach of photon migration is advantageous to the standard diffusion theory in several applications, since it offers important physical insight into the problem and simple mathematical solutions. Because of its importance, we devote this entire Chapter to the discussion of the photon migration approach, including a review of the background of tissue turbidity, current research approaches in modeling light propagation in turbid media, and various applications of photon migration in biomedical diagnostics and imaging. In particular, we explore its application to modeling the effects of boundary conditions, which will become extremely useful in the inverse algorithm used to extract the spatial information about embedded fluorescent objects using a time-resolved tomographic scheme, Chapter 4.

2.1 Radiative Transfer Equation, Diffusion Approximation and Photon Migration

The understanding of light propagation in turbid media is essential in disease diagnosis and medical imaging using optical/spectroscopic techniques [Chance & Alfano, 1995; Alfano & Fujimoto, 1996]. Light propagation in tissue is governed by the probabilistic scattering and absorption of photons by the tissue. In the approximation in which the wave properties of light are neglected, this process can be described by the radiative transfer equation [Ishimaru, 1978].

Because the solution to the integro-differential radiative transfer equation is usually not available, the diffusion approximation has been a standard approach to modeling the light propagation in turbid media [Ishimaru, 1978]. In the NIR range, the tissue absorption coefficient (μ_a on the order of 0.001-0.01 mm^{-1}) is very small compared to the tissue scattering coefficient (μ_s on the order of 10 mm^{-1}). Despite the fact that the tissue scattering is usually highly forward (i.e., the anisotropy coefficient, i.e., the average cosine of single scattering angle, θ, $g = <cos\theta> \sim$ 0.9-0.95), the reduced scattering coefficient ($\mu_s'=\mu_s(1-g)\sim 1$ mm^{-1}) is still much greater than the absorption coefficient, which makes the diffusion theory an appropriate approximation for many biomedical applications [Chance & Yodh, 1995]. The steady-state diffusion theory has long been used in interpreting multiple scattered light from turbid media [Ishimaru, 1978; Van de Hulst, 1980]. The application of time-dependent diffusion theory to time-resolved spectroscopy and optical imaging has been pioneered by Patterson *et al* [Patterson *et al*, 1989]. Thereafter, numerous research works, varying from basic theoretical analysis [O'Leary *et al*, 1992; Schotland *et al*, 1993] to more clinically oriented applications

[Peters *et al*, 1990; Sevick *et al*, 1991], have been reported to extract spectroscopic information and to image inhomogeneities embedded in turbid media using the diffusion approximation. Although this approach has enjoyed a great popularity, its limitations have also been noted. In particular, the diffusion approximation is inaccurate at short times, at the positions close to the source and/or boundary, and for small inhomogeneities. In addition, although the solution of the diffusion equation is well known in an infinite medium, in many practical situations the physical boundary conditions often preclude a simple determination of the solution.

The diffusion approximation, in a sense, describes the ensemble average of probabilistic photon scattering and absorption at each spatial point within the turbid media. Alternatively, the photon migration picture, introduced by Bonner and coworkers [Bonner *et al*, 1987], has been explored to solve the same problem. It models the light propagation in turbid media as the ensemble average of the *probabilistic photon migratory paths* distributed within the turbid media; and the realization of the full path of each individual photon is governed by the scattering and absorption properties [Wu, 1992], as well as the boundary conditions of the medium (see below). Although fundamentally equivalent to the radiative transfer equation, photon migration offers a diagrammatic approach which can provide important new physical insights into specific problems. In particular, the concept of photon path is extremely useful in optical imaging applications, since it reveals a direct correlation between the optical signal detected on the surface and the internal structure probed by the photons traversing the medium. Both random walk theory and the path integral approach have been explored to provide

mathematical descriptions of this picture [Nossal *et al*, 1989; Perelman *et al*, 1994]. In addition, Monte Carlo simulation of the radiative transfer equation, because of its statistic nature in recording individual photon histories in the medium, has been a very important investigation tool and has been used as the gold standard in photon migration studies. The Monte Carlo code used in this thesis study has been examined against standard results [Prahl, 1988] and described in details in my master thesis and elsewhere [Wu, 1992; Wu *el al*, 1993a].

2.2 Diffuse Reflectance and Fluorescence in Turbid Media: A Review

As detailed in my master thesis [Wu, 1992], the photon migration approach has been successfully applied to modeling the diffuse reflectance and fluorescence from turbid media, and it has provided simple and accurate solutions in these cases. The purpose of this review is to give a flavor for the wide applications offered by the photon migration picture.

Diffuse reflectance is known to depend on the optical parameters of the medium, and theoretical modeling of the diffuse reflectance and the inverse extraction of the optical parameters are important issues in both spectroscopic diagnosis and optical tomographic imaging. In the photon migration picture an individual photon path can be described by the number of scattering events and their realization probability, and therefore a probability distribution function that a photon will escape from the tissue after certain number of scattering events can be introduced based on the understanding of the photon migration in turbid media [Wu *et al*, 1993a]. This approach provides both

accuracy and simplicity in diffuse reflectance calculations for a wide range of scattering, absorption and anisotropy coefficients typically found in human tissue. First, it allows the separation of the phase dependence of scattering from the single scattering albedo, thus greatly simplifying the modeling of diffuse reflectance. In addition, it leads the discovery of a universal probability function which allows the diffuse reflectance from any type of tissue to be described by a single, invertable equation. Last, the diffuse reflectance calculated analytically by this method is in excellent agreement with the results of Monte Carlo simulations over the wide range of optical parameters typically found in human tissue. This is demonstrated in Fig. 2.1, which compares the photon migration results (continuous lines) with Monte Carlo simulations (discrete points) for various optical parameters of the medium.
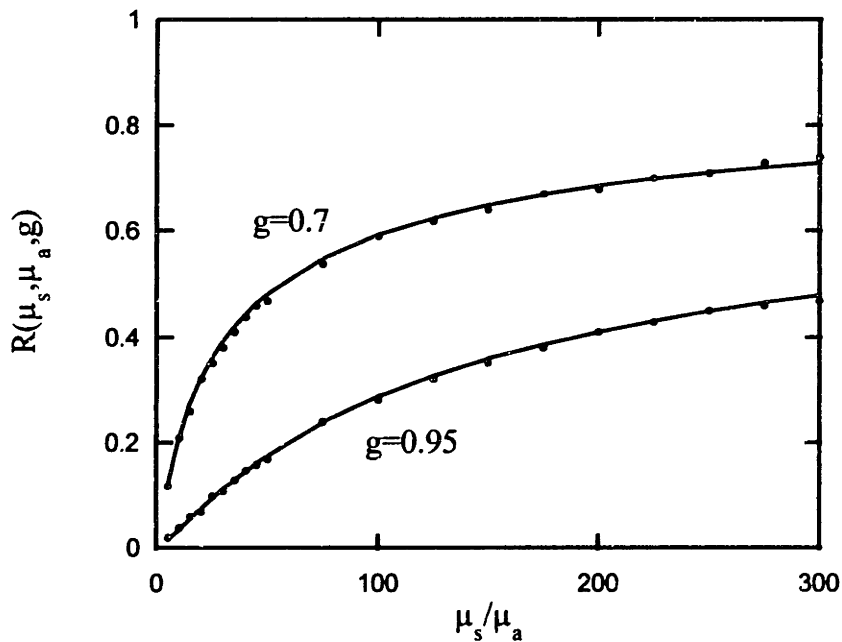
Figure 2.1. Comparison between the Monte Carlo simulations and the photon migration model for the diffuse reflectance in a turbid medium.

Likewise, in modeling tissue fluorescence the photon migration picture provides an important physical insight and reveals the underlying similarity between diffuse reflectance and fluorescence in optically thick turbid media such as human tissues [Wu *et al*, 1993b]. In such a medium the intrinsic fluorescence lineshape of the fluorophores is distorted by an interplay of many factors, including scattering and absorption, excitation and collection geometries, and boundary conditions. Thus, it is essential to correctly interpret the measured fluorescence spectra so that it can be compared to the individual tissue fluorophore spectra obtained from microscopic studies using thin tissue slices. Here, the physical insight provided by the photon migration picture leads to a novel method of removing spectral distortions precisely, thus providing a means of extracting the intrinsic tissue fluorescence by taking the ratio of the measured fluorescence to the diffuse reflectance obtained in the same manner. The validity of this approach has been examined by both laboratory experiments on human aortic media and comparison with Monte Carlo simulations [Wu, 1992]. For example, Fig. 2.2(a) plots the measured diffuse reflectance and the fluorescence spectra from an aortic medium sample with high hemoglobin content. By applying the photon migration model, the effects of distortion are completely removed to yield the intrinsic tissue fluorescence spectrum, as measured from a thin slice of the same tissue sample, Fig. 2.2(b). Therefore, this model allows the accurate extraction of the physico-chemical information of tissue composition in clinical applications of spectroscopic diagnosis, and thus provides biochemical and morphological information about tissue pathology.

14
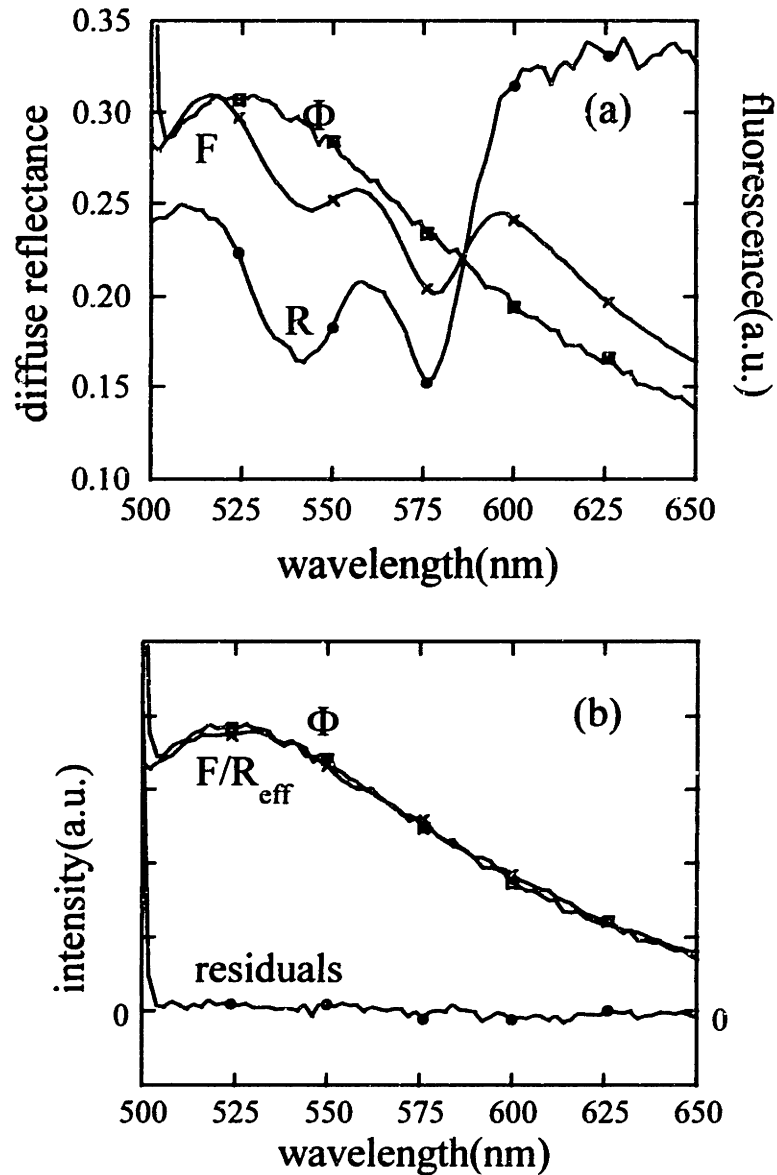
Figure 2.2. Experimental data from human aortic media soaked in lysed blood. (a) Comparison of the optically thick fluorescence (crosses), reflectance (circles), and thin fluorescence (squares). (b) Comparison of the intrinsic fluorescence extracted by using the photon migration model (crosses) and measured from thin sample (squares); residuals (circles) are included.

2.3 Boundary Condition Problems: A Convolution Picture and Its Implications

In this section the application of the photon migration picture to boundary condition problems of light propagation in turbid media is presented. This work is important not only because it provides a new understanding of the physical picture of the boundary effects, but also because it suggests a convenient mathematical model that can be incorporated into the inverse algorithm used in the prototype tomographic system (Chapter 4).

In most non-invasive optical diagnosis, the tissue-air interface introduces discontinuities of both the scattering/absorption properties and the refractive index, which significantly change the optical signals being detected on the boundary. It is well known that both the spectral lineshapes (in studies of spectroscopic diagnosis) and the temporal profiles (in optical imaging studies) are strongly affected by the boundary conditions. In order to extract accurate spatial information about the internal structures using non-invasive time-resolved measurements on the surface, it is essential to properly describe the effects of the tissue-air interface and correctly include the boundary conditions in the inverse algorithms.

As will be shown below, based on the photon migration approach the boundary conditions can be written in the form of a *spatio-temporal* convolution. This result, especially its *temporal* part, is very appealing because of its physical elegance and, more importantly, its potential application to time-resolved optical imaging. In Chapter 4 of this thesis a multi-channel tomographic technique will be presented to locate fluorescence objects deeply embedded in a turbid medium by measuring the time-dependent

fluorescence signals on the boundary between the medium and the air. In this situation, the convolution approach to modeling the medium-air boundary allows us to separate the fluorescent source-dependent term (which can be shown to be identical to the solution in an infinite medium) from the boundary-dependent term (which physically represents the Green's function for a secondary source at the boundary, and is thus independent of the original fluorescent source) in some common situations. Since the latter term is the same for all the detection channels, the boundary condition effect cancels by taking the ratio between two channels in the Laplace or Fourier transform space. Also, because of the cancellation, this approach does not require specific knowledge of the nature of the boundary, such as an index-matched vs. an index-mismatched boundary. Therefore, the information about the embedded fluorescent objects can be accurately obtained by simply using the solution in an infinite medium, which is much easier to obtain [Carslaw & Jaeger, 1959].

Most of the following discussions are restricted to boundary conditions in a semi-infinite geometry, which is a good approximation in most tomographic imaging studies, considering that both the sample thickness as well as the surface curvature are typically much greater than the transport mean free path. In addition, in the semi-infinite geometry the physical picture and the mathematics are much simpler and more straightforward than other geometries, such as a curved surface or a slab with more than one surfaces. In particular, we are interested in observation of an embedded emission source by a detector at the boundary, which is appropriate to model the photon migration of the fluorescence

emission from the embedded fluorescent object to the optical fiber located at the medium boundary in the prototype tomographic system (Chapter 4).

In the following sections, we first briefly review some of the standard methods to solve boundary condition problems [Glasstone, 1955; Keijzer et al, 1988; Patterson et al, 1989; Haskell et al, 1994; Aronson, 1995], most of those developed under the framework of diffusion theory. We will then describe the diagrammatic photon migration approach to this problem and present a simple method of removing the boundary effects in time-resolved measurements by using Laplace/Fourier transformations.

Standard Approaches to Solving Boundary Condition Problems

The diffusion equation in an infinite medium is in general written as an equation of the photon fluence rate, U:

$$\frac{\partial U(\vec{r},t)}{c\partial t} - D\nabla^2 U(\vec{r},t) + \mu_a U(\vec{r},t) = \delta(z-z_0)\delta(\vec{\rho})\delta(t) \tag{2.1}$$

where $\vec{r} = (\vec{\rho}, z)$ is the 3-dimensional position vector, $\vec{\rho}$ is the 2-D radial coordinate in the boundary plane, and z is the depth into the medium, $\delta(z-z_0)\delta(\vec{\rho})\delta(t)$ describes the isotropic emission source at z_0, and $D = \frac{1}{3\mu_s'}$. Note that in the diffusion approximation the scattering coefficient, μ_s, and the anisotropy coefficient, g, are grouped into a single parameter, the reduced scattering coefficient, μ_s' [Ishimaru, 1978].

In a semi-infinite medium, a boundary condition has to be added to Eq. 2.1.a. One standard approach is to write an approximate equation for the photon fluence rate, U, at the boundary [Glasstone, 1955; Ishimaru, 1978]. This leads to the so-called *partial current boundary condition* which assumes that light leaving the scattering medium

through the tissue-air interface does not return to the medium. Mathematically it is written as a mixed Dirichlet-Neuman boundary condition, i.e., the sum of the fluence rate and its derivative is zero at the boundary:

$$hU(\vec{r},t) = \frac{\partial U(\vec{r},t)}{\partial z} \quad \text{at } z = 0 \tag{2.1.a}$$

where $h = \frac{1-R_{\text{eff}}}{1+R_{\text{eff}}} \frac{1}{2D}$, with R_{eff} depending on the refractive index-mismatch at the boundary [Groenhuis *et al*, 1983].

Because boundary condition problems of this form are hard to solve, an *extrapolated boundary condition* has been proposed [Glasstone, 1955]. Mathematically it is written in the form of Dirichlet boundary condition, i.e., the fluence rate equals zero at an extrapolated boundary, z_b, whose exact location depends on the interface mismatches in both the scattering coefficient and the refractive index:

$$U(\vec{r},t) = 0 \quad \text{at } z = -z_b = -\frac{1}{h}. \tag{2.1.b}$$

This Dirichlet boundary condition problem can be solved relatively easily by invoking the method of image sources.

Under further approximation, Patterson *et al* [Patterson *et al*, 1989] simplified the boundary condition to the so-called *zero boundary condition* in which the fluence rate is set equal to zero at the tissue-air interface:

$$U(\vec{r},t) = 0 \quad \text{at } z = 0 \tag{2.1.c}$$

Because of the great mathematical simplicity, this approximation is most widely used in studies of photon diffusion in tissue. However, refractive-index mismatch at the boundary is not incorporated into this method.

Physical Picture Of Photon Migration

It has been noted that all of the above approaches fail to provide important physical insights to the boundary condition problems. Alternatively, photon migration can provide a diagrammatic approach to solve this problem. Generally speaking, the boundary conditions in photon migration can be schematically diagrammed as in Fig. 2.3. In Fig. 2.3(a), the medium is infinite, the detector plane is at an imaginary boundary, $z=0$, with identical media on both sides, and a light source is located somewhere in the lower half of the medium, at z_0. In Fig. 2.3(b), the location of the source and the scattering/absorption properties of the medium are the same as in Fig. 2.3(a), except that there is a tissue-air boundary at the detector plane. Here, for the time being, an index-matched boundary is assumed. According to the photon migration picture, in the case of a semi-infinite medium, Fig. 2.3(b), all the photon paths are terminated once the photons arrive at the detector plane, $z=0$, for the first time, since after their crossing the boundary photons undergo no further scattering and thus can never return to the medium. However, in an infinite medium, Fig. 2.3(a), on the one hand, the photons can be detected at the detector plane just as they can in a semi-infinite medium; on the other hand, in the infinite medium they continue undergo scattering. Notice that before the photons arrive at the boundary for the first time, statistically they migrate over the same trajectories as those in the semi-infinite medium from the original source to the boundary plane;

whereas during their continued travel, the additional paths are governed by the optical properties of the medium, but are *independent* of the position of the original light source. Thus, we can treat the point at which the photon arrives at the boundary for the first time, *B*, as a secondary emission source, so that the detected signal in the infinite medium can be viewed as composed of two parts: the semi-infinite path from the original source $(z=z_0)$ to the detector at the boundary $(z=0)$ and the infinite path from the secondary source at the boundary $(z=0)$ to the detector at the boundary $(z=0)$. Note in general the secondary source equals the semi-infinite response multiplied by a *boundary condition operator* (see Appendix at the end of this Chapter). Mathematically, the detected signal in the infinite medium can be written as the convolution of two terms, with the first one identical to the detected signal in the semi-infinite medium and the second term fully determined by the optical properties of the medium and the specific form of the boundary condition (i.e., the boundary condition operator), but independent of the position of the original light source. Note that, in general, this convolution must be taken both temporally (*t*) and spatially ($\vec{\rho}$) over the boundary surface.

Similarly, an index-mismatched boundary can be treated in a like manner. In Fig. 2.3(c), an index-mismatched boundary is placed at the surface of the semi-infinite medium. When compared to Fig. 2.3(b), some of the photon paths (the internal reflection part determined by the Fresnel's equations, which defines the boundary condition operator in this case) continue, whereas others (the transmitted part) are terminated. Similar to the infinite medium situation, the index-mismatched boundary condition can also be treated as a two-term convolution.
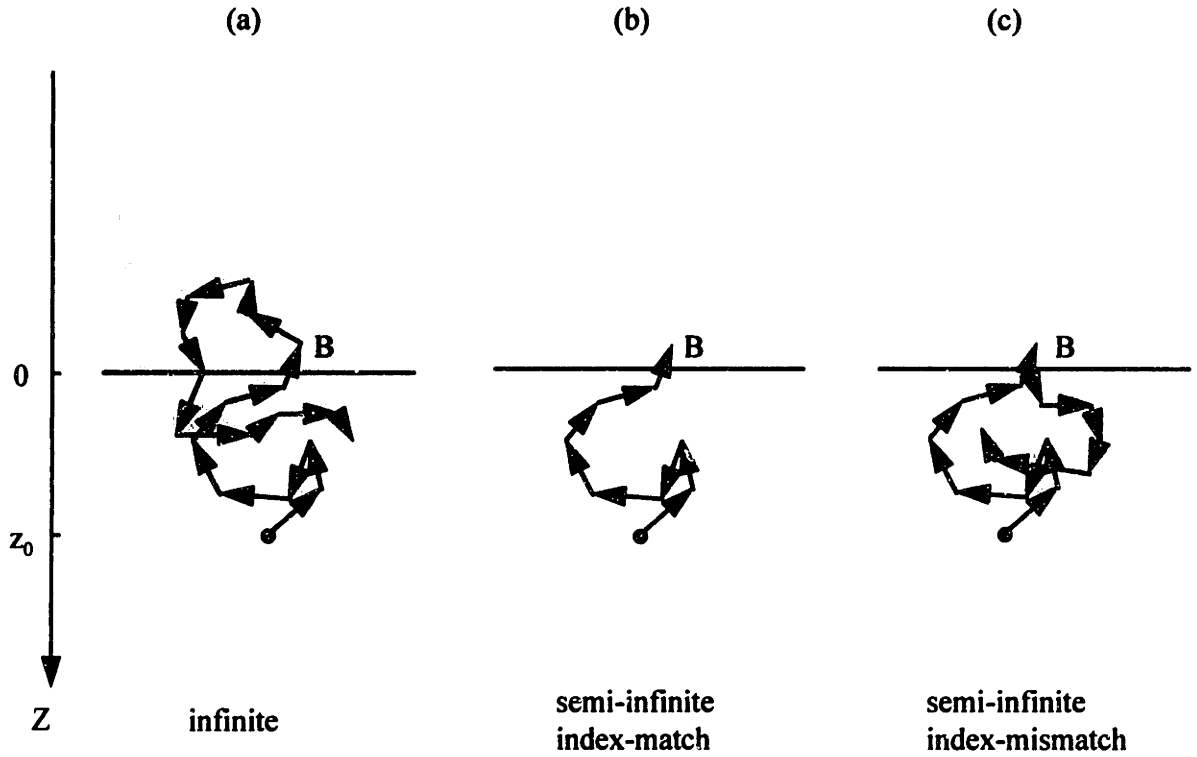
Figure 2.3. Schematic diagrams of the boundary conditions in photon migration. (a) an infinite medium, (b) an index-matched, semi-infinite medium, and (c) an index-mismatched, semi-infinite medium.

Therefore, these typical boundary condition problems can be formulated in terms of convolution integrals:

$$U_{\text{infinite}}(t,\vec{p},z_0) = U_{\text{semi-infinite}}^{\text{index-match}}(t,\vec{p},z_0) \otimes G_{\text{infinite}}(t,\vec{p}),$$ (2.2.a)

and

$$U_{\text{semi-infinite}}^{\text{index-mismatch}}(t,\vec{p},z_0) = U_{\text{semi-infinite}}^{\text{index-match}}(t,\vec{p},z_0) \otimes G_{\text{semi-infinite}}^{\text{index-mismatch}}(t,\vec{p}),$$ (2.2.b)

where U is the photon fluence rate in the turbid medium, $\vec{p}$ is the radial coordinate in the plane of the boundary, and $\otimes$ denotes the convolution operator. Note that the G terms

are independent of the original source. Physically, they represent the sum of a δ-function component (the semi-infinite response, in addition to determining the secondary source, also contributes to the detection), and the Green's function component of the secondary emission source on the boundary (as determined by the semi-infinite response and the boundary condition operator). It should be mentioned that the angular distribution of the photons has been ignored. This is consistent with the assumption of the diffusion approximation that, in highly turbid media, the photons are randomly scattered so that the angular distribution is more or less isotropic. More generally, when the exact angular distribution is also considered [Van de Hulst, 1980], the above picture has to be modified to include an angular convolution as well.

The convolution integrals, Eq. 2.2.b, can be greatly simplified by using the Laplace transform,

$$\tilde{A}(s) = \int_0^{+\infty} A(t)\exp(-st)dt, \tag{2.3.a}$$

or the Fourier transform,

$$\tilde{A}(\omega) = \int_{-\infty}^{+\infty} A(t)\exp(-i\omega t)dt, \tag{2.3.b}$$

taking advantage of the well known convolution theorem [Sokolnikoff & Redheffer, 1966], which states that when two functions are convolved, the Laplace (Fourier) transform of the convolution is just the product of the individual Laplace (Fourier) transforms. In boundary condition problems, we are interested in the situation in which the two functions are convolved both temporally and spatially. For the temporal part, we shall focus on the Laplace transform, since it is more appropriate in deriving the inverse

algorithm of using early arriving photons to probe embedded fluorophores (see Chapter 4). However, all the principles should be equally applicable to the Fourier transform. Thus, this convolution picture is equally useful in describing frequency domain optical imaging studies [Chance & Alfano, 1995; Alfano & Fujimoto, 1996]. Since the spatial Laplace transform is not well defined, the Fourier transform will be used for the spatial part. However, it will be shown later that in some practical situations, the spatial part is not important and thus can be ignored.

Considering the convolution theorem, Eqs. 2.2.a and 2.2.b become:

$$\tilde{\tilde{U}}_{\text{infinite}}(s,\omega,z_0) = \tilde{\tilde{U}}^{\text{index-match}}_{\text{semi-infinite}}(s,\omega,z_0) \bullet \tilde{\tilde{G}}_{\text{infinite}}(s,\omega),$$
(2.4.a)

and

$$\tilde{\tilde{U}}^{\text{index-mismatch}}_{\text{semi-infinite}}(s,\omega,z_0) = \tilde{\tilde{U}}^{\text{index-match}}_{\text{semi-infinite}}(s,\omega,z_0) \bullet \tilde{\tilde{G}}^{\text{index-mismatch}}_{\text{semi-infinite}}(s,\omega),$$
(2.4.b)

where the double tilde denotes the Laplace/Fourier transformation in both temporal and spatial dimensions with s and ω the Laplace (temporal) and Fourier (spatial) parameters, respectively. Equations 2.4.a and 2.4.b can be combined as:

$$\tilde{\tilde{U}}_{\text{infinite}}(s,\omega,z_0) = \tilde{\tilde{U}}_{\text{semi-infinite}}(s,\omega,z_0) \bullet \tilde{\tilde{G}}(s,\omega)$$
(2.4.c)

or

$$\tilde{\tilde{U}}_{\text{semi-infinite}}(s,\omega,z_0) = \tilde{\tilde{U}}_{\text{infinite}}(s,\omega,z_0) \bullet \tilde{\tilde{G}}'(s,\omega)$$
(2.4.d)

with G (G') redefined accordingly. Note that such redefinition is possible because the convolution becomes simple multiplication in the Laplace/Fourier transform space.

In summary, we present a photon migration picture of the boundary condition problems, which suggests that the boundary condition problem of a semi-infinite medium

is related to the problem of an infinite medium through a second convolution term independent of the original light source, Eq. 2.4. Since the solution to the problem of an infinite-medium is more readily available, this approach provides a convenient alternative way to handle boundary condition problems.

Although, in general, the G terms exhibit both temporal and spatial dependence, the temporal part is more interesting in time-resolved optical imaging applications where the temporal profiles carry important spatial information about the internal structure of the medium. There, the temporal convolution can be easily handled by applying the Laplace transformation to the time-resolved signals. However, since mathematically the spatial and the temporal parts are tangled together in the G terms, it greatly complicates the transformation analysis and requires the spatio-temporal Laplace/Fourier transform procedure. Fortunately, under certain circumstances, the spatial part can be shown to asymptotically approach a constant. A simple temporal Laplace transformation can then lead to the clean separation of the source-dependent term from the boundary-dependent term.

In the following sections, we first validate this convolution picture by using standard diffusion theory solutions. The situation of a plane source is discussed first. Since there is no explicit spatial dependence on the boundary, a simple temporal Laplace transformation approach is used to demonstrate the convolution nature of the boundary condition. We then proceed to the case of a point source, where we use a spatio-temporal transformation to validate this picture. We further discuss the use of a temporal Laplace transformation for the point source problem, which is most relevant to the experiments of

using time-resolved tomographic technique to detected embedded fluorophores, i.e., the point emission sources, inside a turbid medium (see Chapter 4 of this thesis). Lastly, we will discuss the potential error introduced by using a temporal, instead of a spatio-temporal, transformation as well as the conditions under which the spatial part becomes invariant so that the error is negligible.

<u>One-Dimensional Problem (A Plane Source) - Temporal Laplace Transform</u>

Consider the simple situation of a plane source at $z=z_0$ inside a semi-infinite medium., where the solution at the boundary ($z=0$) has no explicit spatial dependence. Therefore, it is expected that the solution with the boundary condition (a semi-infinite medium) is simply a temporal convolution of the solution without the boundary condition (an infinite medium) and a second source-independent term. Here, the diffusion equation for the infinite medium is given as Eq. 2.1. For the semi-infinite medium with a generalized boundary condition (either index-matched or index-mismatched), the diffusion equation with boundary condition is given in Eqs. 2.1 and 2.1.a. Note for a plane source, the source term is $\delta(z - z_0)\delta(t)$.

In fact, in this situation, the equations can be more easily solved using the temporal Laplace transform. The solution for the infinite medium is [Carslaw & Jaeger, 1959]:

$$
\begin{aligned}
\widetilde{U}_{\text{infinite}}(\vec{r}, s) &= \frac{c}{2\sqrt{Dc(s + \mu_a c)}} \exp(-\sqrt{(s + \mu_a c)/Dc}|z - z_0|) \\
&= \frac{c}{2kq} \exp(-q|z - z_0|),
\end{aligned}
$$

(2.5.a)

where $k = Dc$, and $q = \sqrt{(s + \mu_a c)/Dc}$. At the boundary ($z=0$), Eq. 2.5.a reduces to

$$\tilde{U}_{\text{infinite}}(z=0,s) = \frac{c}{2kq}\exp(-qz_0).$$

(2.5.a')

For the semi-infinite medium, the solution is given by [Carslaw & Jaeger, 1959]:

$$\tilde{U}_{\text{semi-infinite}}(\vec{r},s) = \frac{c}{2kq}\{\exp(-q|z-z_0|) + \exp(-q(z+z_0))\}$$

$$-\frac{hc}{kq(q+h)}\exp(-q(z+z_0)),$$

(2.5.b)

which is equal to

$$\tilde{U}_{\text{semi-infinite}}(z=0,s) = \frac{c}{2kq}\exp(-qz_0)\{2 - \frac{2h}{q+h}\},$$

(2.5.b')

at the boundary. Note that at the boundary $\tilde{U}_{\text{semi-infinite}}$ is written as a product of $\tilde{U}_{\text{infinite}}$ and a second term dependent on the boundary condition (the h-dependent factor) but independent of the original source (i.e., z_0-independent). Thus, it is proved that an generalized boundary condition (index-matched or index-mismatched) can be re-formulated as a temporal convolution term.

Three-Dimensional Problem (A Point Source) - Temporal Laplace Transform And Spatial Fourier Transform

In the case of a point source inside a semi-infinite medium, the G term has both explicit temporal and spatial dependence. In order to validate the convolution picture, it is necessary to apply the Laplace/Fourier transform in both the temporal and spatial dimensions. Here the diffusion equations are given by Eq. 2.1 (for an infinite medium) and Eqs. 2.1 and 2.1.a (for a semi-infinite medium). Again the solutions are given by Carslaw & Jaeger [Carslaw & Jaeger, 1959]:

27

$$U_{\text{infinite}}(t, z = 0) = c(4\pi Dct)^{-3/2} \exp\left(-\frac{\rho^2 + z_0^2}{4Dct} - \mu_a ct\right),$$ (2.6.a)

and

$$U_{\text{semi-infinite}}(t, z = 0) = c(4\pi Dct)^{-3/2} \exp\left(-\frac{\rho^2}{4Dct} - \mu_a ct\right) \times$$

$$\times \left\{2\exp\left(-\frac{z_0^2}{4Dct}\right) - 2h\int_0^{+\infty} \exp\left(-hl - \frac{(z_0 + l)^2}{4Dct}\right)dl\right\}$$ (2.6.b)

Applying the Laplace transform to the temporal part, exp*(-st)*, and the Fourier transform

to the spatial part, exp*(-iω_xx-iω_yy)*, Eqs. 2.6.a and 2.6.b become:

$$\tilde{\tilde{U}}_{\text{infinite}}(s, \omega_x, \omega_y, z = 0) = \frac{c}{\sqrt{4Dc}\sqrt{\mu_a c + s + 16Dc(\omega_x^2 + \omega_y^2)}} \times$$

$$\times \exp\left(-\sqrt{\mu_a / D + s / Dc + 16(\omega_x^2 + \omega_y^2)}\, z_0\right),$$ (2.7.a)

and

$$\tilde{\tilde{U}}_{\text{semi-infinite}}(s, \omega_x, \omega_y, z = 0) = \frac{c}{\sqrt{4Dc}\sqrt{\mu_a c + s + 16Dc(\omega_x^2 + \omega_y^2)}} \times$$

$$\times \exp\left(-\sqrt{\mu_a / D + s / Dc + 16(\omega_x^2 + \omega_y^2)}\, z_0\right) \times$$ (2.7.b)

$$\times \left(2 - \frac{2h}{h + \sqrt{\mu_a / D + s / Dc + 16(\omega_x^2 + \omega_y^2)}}\right).$$

Thus, it is clear that in 3-D cases the semi-infinite medium solution can also be written as

the convolution of the infinite medium solution and a second term which is independent

of the original light source, i.e.,

$$\tilde{\tilde{U}}_{\text{infinite}}(z_0) = \tilde{\tilde{U}}_{\text{semi-infinite}}(z_0) \bullet \tilde{\tilde{G}}$$ (2.7.c)

where $\tilde{\tilde{G}} = \left(2 - \dfrac{2h}{h + \sqrt{\mu_a / D + s / Dc + 16(\omega_x^2 + \omega_y^2)}}\right)^{-1}$.

It is interesting to note that in the special case in which $h = 0$ ($R_{eff} = 1$), i.e., the refractive index-mismatch is infinite, all the photons arriving at the boundary will be reflected back to the medium due to internal reflection. In other words, the boundary is like a mirror and all the scattering/absorption events in the semi-infinite medium can be viewed as either identical to or the mirror images of their counterparts in the infinite medium, i.e., the mirror concentrates all the photons within the half-space, and thus doubles the local fluence rate at the boundary. Therefore, Eq. 2.7.c, in this special case, becomes $\tilde{\tilde{U}}_{semi-infinite} = 2\tilde{\tilde{U}}_{infinite}$.

More interestingly, if the same analysis is applied to the diffusion solution with the zero boundary condition [Patterson et al, 1989], in which the fluence rate is assumed zero and the photon flux is measured at the boundary of the semi-infinite medium:

$$U_{infinite}(t,z = 0) = c(4\pi Dct)^{-3/2}\exp(-\frac{\rho^2 + z_0^2}{4Dct} - \mu_a ct),$$ (2.8.a)

and

$$U_{semi-infinite}(t,z = 0) = \frac{z_0}{t}(4\pi Dct)^{-3/2}\exp(-\frac{\rho^2 + z_0^2}{4Dct} - \mu_a ct),$$ (2.8.b)

we obtain:

$$\tilde{\tilde{U}}_{infinite}(s,z = 0)$$
$$= \frac{c}{2\sqrt{Dc(s + \mu_a c + 16Dc(\omega_x^2 + \omega_y^2))}}\exp(-\sqrt{s / Dc + \mu_a D + 16(\omega_x^2 + \omega_y^2)}z_0),$$ (2.9.a)

and

$$\tilde{\tilde{U}}_{semi-infinite}(s,z = 0) = \exp(-\sqrt{s / Dc + \mu_a D + 16(\omega_x^2 + \omega_y^2)}z_0).$$ (2.9.b)

Thus the boundary-dependent term is $\widetilde{G} = \dfrac{c}{2\sqrt{Dc(s + \mu_a c + 16Dc(\omega_x^2 + \omega_y^2))}}$, and its

inverse Laplace/Fourier transform yields $G(t) = c(4\pi Dct)^{-3/2} \exp(-\dfrac{\rho^2}{4Dct} - \mu_a ct)$, which

is the same as Eq. 2.8.a with $z_0 = 0$. It therefore represents a secondary emission source at

the boundary. Note that this simplified mathematical model provides a clear physical

picture: the photon migration from the source, $z=z_0$, to the detector plane, $z=0$, in an

infinite medium is equivalent to a two-part process with the first part identical to the

photon migration from $z=z_0$ to $z=0$ in a semi-infinite medium and the second being that

from $z=0$ to $z=0$ in an infinite medium. Also note that under this special approximation,

the δ-function component in the second term is zero (the zero boundary condition) and

the boundary condition operator is a unit operator (no index-mismatch at the boundary).

Three-Dimensional Problem (A Point Source) - Temporal Laplace Transform Only

Strictly speaking, in the 3-D case a simple temporal Laplace transformation

cannot separate the source-dependent term from the boundary-dependent term

completely. This can be seen by applying only the temporal Laplace transform to Eqs.

2.6.a and 2.6.b. Here we can write:

$$\widetilde{U}_{\text{infinite}}(z_0) = \widetilde{U}_{\text{semi-infinite}}(z_0) \bullet \widetilde{G}(z_0) \qquad (2.10)$$

where $\widetilde{G} = \{2 - 2h \displaystyle\int_0^{+\infty} \sqrt{\dfrac{\rho^2 + z_0^2}{\rho^2 + (l + z_0)^2}} \exp(-hl - q(\sqrt{\rho^2 + (l + z_0)^2} - \sqrt{\rho^2 + z_0^2}))dl\}^{-1}$ and

$q = \sqrt{(s + \mu_a c)/Dc}$. Note that $\widetilde{G}$ is not independent of z_0. However, as will be shown

below, the spatial dependence becomes less important when the source is not very close

to the boundary. This is because as the light source becomes deeper and deeper, the

spatial profile on the surface becomes more and more uniform (approaching to the plane source situation). In order to find this critical depth, numerical calculations were performed using both the diffusion equation and Monte Carlo simulations. Ideally, it is desired that under certain circumstances the $\tilde{G}$ term becomes independent of the emission source, i.e., z_0-independent.

The $\tilde{G}$ term was first evaluated numerically using Eq. 2.10. Here the typical scattering and absorption coefficients found in human breast tissue at 800 nm [Mitic *et al*, 1994] were used: $D = 0.33$ mm ($\mu_s' = 1.0$ mm^{-1}), $\mu_a = 0.005$ mm^{-1}, and $h = 0.5$ (n_{tissue}/n_{air} $= 1.36$). Fig. 2.4 shows the calculation results of $\tilde{G}$ as a function of s for the cases of source position $z_0 = 10$, 25, and 40 mm, $\rho = 0$ mm and the detector position $\rho = 0$ mm at the boundary. Notice that as the source becomes deeper, the curves begin to cluster. This can also be seen from Fig. 2.5, which plots $\tilde{G}$ as a function of z_0 for the cases of the detector position $\rho = 0$, 5, 10 mm on the surface and $s = 6$ ns^{-1} (a typical value used in the data analysis, Chapter 4). Note that $\tilde{G}$ asymptotically approaches a constant value as z_0 goes to infinity, and at $z_0 = 10$ mm $\tilde{G}$ is not more than 15% from its asymptotic value. These results indicate that as long as the embedded source is deeper than 10 mm below the surface, the boundary condition can be modeled as a temporal convolution term independent of the original source with an error less than 15%. In other words, in time-resolved optical imaging of deep embedded objects, the boundary-dependent convolution term will cancel if the time-resolved signals are Laplace transformed and ratios are then taken between two collection channels. Therefore, accurate spatial information can be expected even though an infinite medium-based model is used in the inverse algorithm.

Figure 2.4. $\widetilde{G}$, defined in Eq. 2.10, as the function of s as calculated using the diffusion equation solutions for various values of z_0 (=10, 25, 40 mm)and ρ (=0 mm).
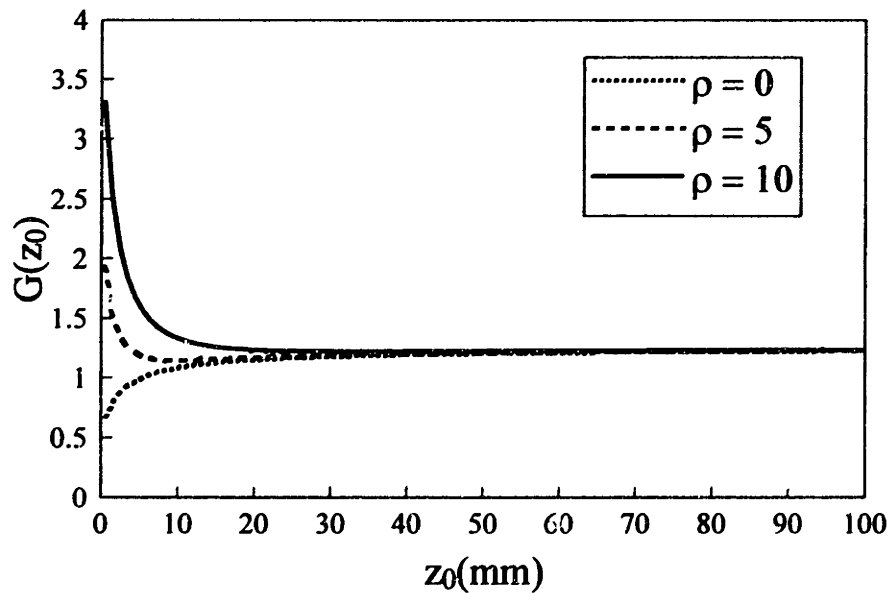
Figure 2.5. $\widetilde{G}$, defined in Eq. 2.10, as the function of z_0 as calculated using the diffusion equation solutions for various values of ρ (=0,5,10 mm) and s =(6 ns^{-1})

Numerical calculations were also performed using the time-resolved Monte Carlo simulations [Wu et al, 1993a] with similar tissue parameters: $\mu_s' = 1.0$ mm^{-1}, $\mu_a = 0.005$ mm^{-1}, and $n_{tissue}/n_{air} = 1.33$. The same three values of z_0 (=10, 25, and 40 mm) and a single value of ρ (=0 mm) were used. In these simulations, one million photons were launched isotropically from the embedded source and the photons leaving the surface of the semi-infinite medium were recorded as a function of time. In processing the data, the temporal Laplace transformation was applied to the time-resolved results from the Monte Carlo simulations for the semi-infinite medium and the diffusion solutions in the corresponding infinite medium, and the ratios were then taken. The results are shown in Fig. 2.6, and similar conclusion can be drawn as above. The statistic error was estimated to be less than 5%, based on multiple calculations.
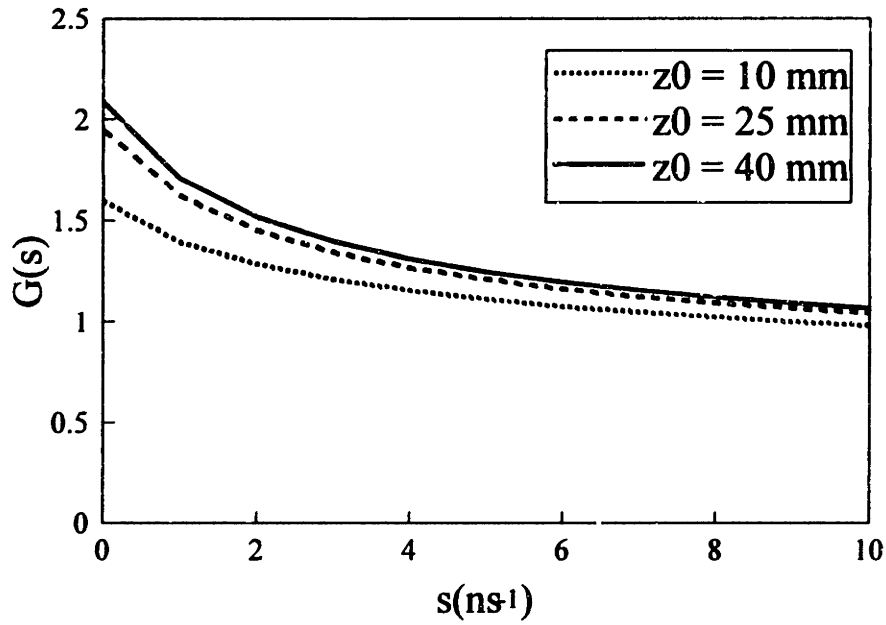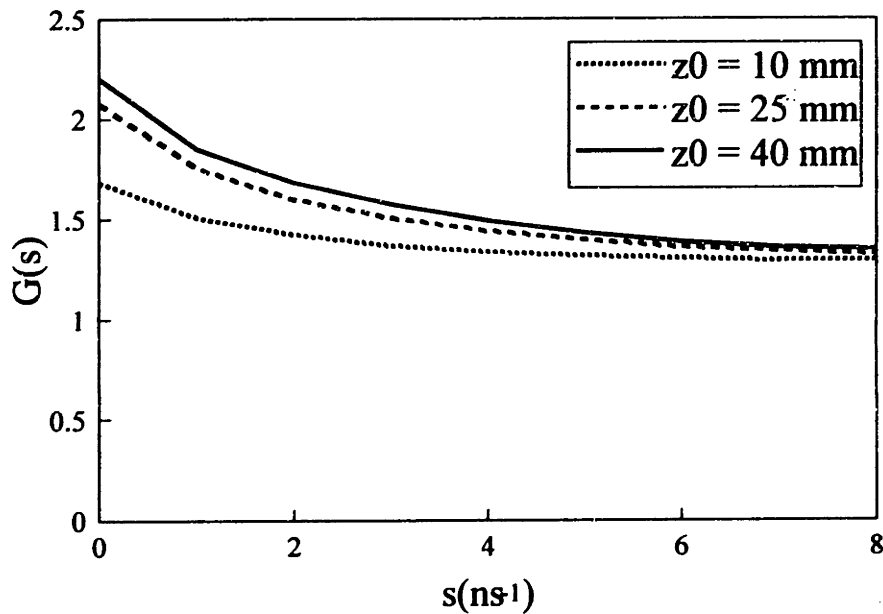

Figure 2.6. $\tilde{G}$, defined in Eq. 2.10, as the function of s as calculated using the Monte Carlo simulations for various values of z_0 (=10, 25, 40 mm) and ρ (=0 mm).

Discussion

In the above, we validated the convolution picture by explicitly writing the diffusion equation solutions for both semi-infinite and infinite media, Eqs. 2.4 through 2.9. In fact, the convolution relation can also be directly derived from the general form of the diffusion equation, Eq. 2.1.a, without explicitly solving it. More interestingly, it can also be derived in a manner analogous to solving the potential problem in QED using Feynman diagrams and Dyson's equation (see Appendix at the end of this Chapter).

Although most of the above discussions have been based on the diffusion approximation, it should be realized that this convolution picture of the boundary conditions in photon migration can be formulated from the radiative transfer equation, and thus goes beyond the diffusion approximation. Therefore, the photon migration approach can also be incorporated into models based on other approaches, such as the Feynman path integral approach [Perelman *et al*, 1994; Perelman *et al*, 1995]. However, when the angular distribution becomes important, a third integral in photon angular distribution must also be included in the convolution.

As mentioned earlier, one important application of this convolution picture is to time-resolved optical tomographic imaging (see Chapter 4 of this thesis). There, the temporal profiles measured by multiple detectors tomographically arranged on the tissue surface contain important spatial information about the internal structures, such as fluorophores embedded in the medium. According to the photon migration picture, the detected signals can be viewed as a temporal convolution of the solution in an infinite medium and a source (i.e., the embedded fluorophore) independent term. Therefore, by

taking the ratio of the Laplace transforms between two channels, all the effects of the tissue-air boundary cancel, and accurate spatial information about the embedded objects can still be obtained by simply using an infinite medium inverse algorithm.

In principle, both the Laplace [Wu *et al*, 1995] and the Fourier [O'Leary *et al*, 1994] transforms can be used in analyzing time-resolved signals, suggesting the usefulness of this convolution picture in frequency domain optical imaging studies as well as in the time domain. However, practically the Laplace transform is more advantageous. This is because the Fourier transformation usually results in strong oscillations in the ratios due to its periodic nature. It becomes especially inaccurate when the denominator term crosses zero. Thus, any small experimental noise, as well as the small error in the spatial convolution term mentioned above, will be magnified in the ratio procedure. On the other hand, the Laplace transformation naturally avoids this problem. Of course the Laplace transformation has its own limitations. For example, it amplifies the noise at very early part of the time-resolved curves. However, this can be avoided by choosing appropriate s values in the analysis [Wu *et al*, 1995].

Although in the above we derived the convolution picture mainly for the purpose of applying it to the tomographic detection of embedded fluorophores, it can also be used to describe the diffuse reflectance/transmission measurements to detect scattering/absorption inhomogeneities embedded in the turbid media, provided that the incident light source and the detector are well separated, i.e., more than 10 mm for the typical breast tissue parameters. In these cases, the incident source should be used instead of the fluorescent source. Since usually the incident source is located on the surface as

well, the boundary condition at the input end of the photon migration paths has to be considered as well. This can be similarly handled in the convolution picture by imagining that the photons migrate backwards from the detector to the source and noting that the photon path probabilities are identical to those of forward photon paths.

Conclusions

In conclusion, this section has presented a convolution picture to model boundary conditions to describe the process of photon migration in turbid media. This approach indicates that the boundary conditions (either index-matched or index-mismatched) can be formulated as a two-term convolution, with the first term identical to the solution in an infinite medium, which can be easily obtained, and a second term independent of the original emission source. In general, the convolution has both temporal and spatial dependence. However, under certain circumstances the spatial part becomes constant, thus the final solution can be cleanly separated into a source-dependent term multiplied by a boundary-dependent term using the temporal Laplace/Fourier transformations. This result is extremely useful in time-resolved optical imaging applications, since it suggests that the boundary condition effects on the time-resolved signals can be removed by taking the ratio between two detection channels in either the Laplace or the Fourier domain, hence that by simply using the solution in an infinite medium, accurate spatial information about the internal structures can still be obtained.

Appendix: Relationship of Photon Migration Treatment to Feynman Diagrams and Dyson's Equation

It is interesting to examine the similarity between the photon migration treatment of the boundary conditions and the Feynman diagram and Dyson's equation methods of solving quantum electrodynamics (QED) problems [Mattuck, 1976]. In QED, the Schrödinger equation with a perturbing potential (V) has the form:

$$(\nabla^2 + i\frac{\partial}{\partial t} - V)G_V = \delta(z - z_0)\delta(\vec{p})\delta(t).$$

$$(\text{A}.1)$$

The solution to this equation, in a Laplace/Fourier transformed domain, may be written using the perturbation expansion [Mattuck, 1976]:

$$\widetilde{G}_V = \widetilde{G}_0 + \widetilde{G}_0 V \widetilde{G}_V = \widetilde{G}_0 + \widetilde{G}_0 V \widetilde{G}_0 + \widetilde{G}_0 V \widetilde{G}_0 V \widetilde{G}_0 + \cdots,$$

$$(\text{A}.2)$$

where each individual term corresponds to one term in the Feynman diagram [Mattuck, 1976]. Equation A.2 can be re-written using Dyson's method [Mattuck, 1976], i.e.,

$$\widetilde{G}_V = \widetilde{G}_0(1 + V\widetilde{G}_V).$$

$$(\text{A}.3)$$

Meanwhile, Eqs. A.2 and A.3 can also be written as

$$\widetilde{G}_0 = \widetilde{G}_V - \widetilde{G}_V V \widetilde{G}_0 = \widetilde{G}_V - \widetilde{G}_V V \widetilde{G}_V + \widetilde{G}_V V \widetilde{G}_V V \widetilde{G}_V + \cdots,$$

$$(\text{A}.2.\text{a})$$

and

$$\widetilde{G}_0 = \widetilde{G}_V(1 - V\widetilde{G}_0).$$

$$(\text{A}.3.\text{a})$$

In an analogous manner, we may re-write the diffusion equation and its boundary condition, Eqs. 2.1 and 2.1.a, for the region $z >= 0$, in a potential form:

$$(-D\nabla^2 + \frac{\partial}{c\partial t} + V)U_{\text{semi-infinite}} = \delta(z - z_0)\delta(\vec{p})\delta(t) + \delta(z + z_0)\delta(\vec{p})\delta(t),$$

$$(\text{A}.4)$$

where $V=2hD\delta(z)$. For simplicity, we ignore the absorption term, which always enters into the solution in the form $\exp(-\mu_a ct)$. That Eq. A.4 is identical to Eqs. 2.1 and 2.1.a can be seen by writing Eq. A.4 for the cases $z>0$ and $z=0$ ($\lim\limits_{\varepsilon \to 0} \int\limits_{-\varepsilon}^{+\varepsilon} dz$) separately.

Now we may define $U^{\pm}_{\text{semi-infinite}}$, so that

$$(-D\nabla^2 + \frac{\partial}{c\partial t} + V)U^{\pm}_{\text{semi-infinite}} = \delta(z \mp z_0)\delta(\vec{\rho})\delta(t).$$ (A.5)

Considering symmetry, $U_{\text{semi-infinite}} = U^+_{\text{semi-infinite}} + U^-_{\text{semi-infinite}} = 2U^+_{\text{semi-infinite}}$ on the boundary $z=0$. Note that Eq. A.5 is the same as the equation for the infinite medium if $V=0$. Following the same treatment leading to Eqs. A.2 and 3, we obtain:

$$\tilde{U}_{\text{infinite}} = \tilde{U}^+_{\text{semi-infinite}}(1 + V\tilde{U}_{\text{infinite}}).$$ (A.6)

Because $V=2hD\delta(z=0)$, Eq. A.6 is

$$\tilde{U}_{\text{infinite}}(z_0 \to 0) = \tilde{U}^+_{\text{semi-infinite}}(z_0 \to 0) \times \{1 + 2hD\tilde{U}_{\text{infinite}}(0 \to 0)\},$$ (A.6.a)

which states that the infinite medium solution is a convolution (multiplication in the transformed domain) of two terms, with the first term identical to the semi-infinite medium solution (except the factor of 2, discussed below) from the original source ($z=z_0$) to the boundary ($z=0$), and the second term independent of the original light source (no z_0 dependence). In addition, the second term consists of a δ-function component and a Green's function component due to the secondary source on the boundary. Lastly, Eq. A.6.a can be shown to be identical to Eq. 2.7.c by applying inverse transformations to the $\tilde{G}$ term, which leads to $G=(1+2hDU_{\text{infinite}}(z0=0))$.

Apparently, Eq. A.6 can also be written in the expanded form:

$$\tilde{U}_{\text{infinite}} = \tilde{U}^{+}_{\text{semi-infinite}} + \tilde{U}^{+}_{\text{semi-infinite}} V \tilde{U}^{+}_{\text{semi-infinite}} + \tilde{U}^{+}_{\text{semi-infinite}} V \tilde{U}^{+}_{\text{semi-infinite}} V \tilde{U}^{+}_{\text{semi-infinite}} + \cdots \quad \text{(A.6.b)}$$

which can be interpreted as the following: the photon path in an infinite medium consists of segments of photon path in a semi-infinite medium, and when the photon path crosses the boundary, it interacts with the boundary via a boundary condition operator, V. (A Feynman diagram of the photon migration boundary condition problem). Here we temporally ignore the factor of 2 difference between the $U_{\text{semi-infinite}}$ and $U^{+}_{\text{semi-infinite}}$. It is interesting to note that with the index-matched boundary condition, $h = \dfrac{1}{2D}$, the boundary condition operator, V, is simply a unit operator, i.e., no changes, either reflection or transmission, occur to the photons when they cross the boundary.

Finally, the factor of 2 appearing in the derivation can be understood physically by realizing that in Eq. A.6.b, U_{infinite} is defined as the total contribution from both sides of the boundary; whereas in the actual physical measurement, it is detected at only one side of the boundary. In other words, photons cannot be detected both above and below the boundary at the same time.

References

R. Alfano & J. Fujimoto, 1996, *Advances in Optical Imaging and Photon Migration TOPS-96*, (OSA, Orlando).

R. Aronson, 1995, "Boundary conditions for diffusion of light," J. Opt. Soc. Am. A, pp 2532.

R. Bonner, R. Nossal, S. Havlin, & G. Weiss, 1987, "Model for photon migration in turbid biological media," J. Opt. Soc. Am., pp 423.

H. Carslaw & J. Jaeger, 1959, Conduction of Heat in Solids, (Oxford University Press, London).

B. Chance & R. Alfano, 1995, *Proceedings of Optical Tomography, Photon Migration, and Spectroscopy of Tissue and Model Media: Theory, Human Studies, and Instrumentation*, SPIE 2389.

S. Glasstone, 1955, <u>Principles of Nuclear Reactor Engineering</u>, (Van Nostrand, New York).

R. Groenhuis, H. Ferwerda, J. Ten Bosch, 1983, "Scattering and absorption of turbid materials determined from reflection measurements, 1: theory," Appl. Opt., 2456.

R. Haskel, L. Svaasand, T. Tsay, T. Feng, M. McAdams, & B. Tromberg, 1994, "Boundary conditions for the diffusion equation in radiative transfer," J. Opt. Soc. Am. A, pp 2727.

A. Ishimaru 1978, <u>Wave Propagation and Scattering in Random Media</u>, (Academic, Orlando).

M. Keijzer, M. Star, & P. Storchi, 1988, "Optical diffusion in layered media," Appl. Opt., pp 1820.

R. Mattuck, 1976, <u>A Guide to Feynman Diagrams in the Many-Body Problems</u>, (McGraw-Hill International Book Company, New York).

G. Mitic, J. Kolzer, J. Otto, E. Plies, G. Solkner, & W. Zinth, 1994, "Time-gated transillumination of biological tissues and tissuelike phantoms," Appl. Opt., pp 6699.

R. Nossal, R. Bonner, & G. Weiss, 1989, "Influence of path length on remote optical sensing of properties of biological tissue," Appl. Opt., pp 2238.

M. Patterson, B. Chance, & B. Wilson, 1989, "Time resolved reflectance and transmittance for the noninvasive measurement of tissue optical properties," Appl. Opt., pp 2331.

V. Peters, D. Wyman, M. Patterson, & G. Frank, 1990, "Optical properties of normal and diseased human breast tissue in the visible and near infrared," Phys. Med. Biol., pp 1317.

S. Prahl, 1988, *Light Transport in Tissue*, Ph.D. thesis, University of Texas at Austin.

J. Schotland, M. Ishii, & J. Leigh, 1993, "Photon hitting density," Appl. Opt., pp 448.

E. Sevick, B. Chance, J. Leigh, S. Nioka, & M. Maris, "Quantitation of time- and frequency-resolved optical spectra for the determination of tissue oxygenation," Anal. Biochem., pp 330.

L. Sokolnikoff & R. Redheffer, 1966, <u>Mathematics of Physics and Modern Engineering</u>, 2nd ed., (McGraw-Hill, New York).

H. Van de Hulst, 1980, <u>Multiple Light Scattering</u>, (Academic Press, Inc., New York).

J. Wu, 1992, *Modeling Light-Tissue Interaction: Applications to Diffuse Reflectance and Fluorescence Spectroscopy of Human Tissue*, Master thesis, MIT, Cambridge.

J. Wu, F. Partovi, M. Feld, & R. Rava, 1993a, "Diffuse reflectance from turbid media: an analytical model of photon migration," Appl. Opt., pp 1115.

J. Wu, M. Feld, & R. Rava, 1993b, "Analytical model for extracting intrinsic fluorescence in turbid media," Appl. Opt., pp 3585.

J. Wu, L. Perelman, R. Dasari, & M. Feld, 1995, "Fluorescence tomographic imaging in turbid media using early arriving photons and Laplace transforms," Proc. Nat. Acad. Sci., submitted.

Chapter 3

Optical Imaging Using Early Arriving Fluorescence Photons: Initial Studies

This Chapter and Chapter 4 describe the experimental aspects of this thesis research, i.e., the use of early arriving fluorescence photon to detect inhomogeneities embedded in highly turbid media. At the beginning of this Chapter, a review of various time-resolved imaging techniques, varying from time domain measurement to frequency domain to coherent methods, is presented. We then present the rationale of our experimental approach, i.e., using early arriving photons for resolution and fluorescence for contrast. In the rest of this Chapter, some initial experiments using early arriving fluorescence to detect embedded objects are presented. In particular, we demonstrate that the long fluorescence lifetime does not obscure the temporal resolution, thus indicating that a good spatial resolution can be achieved. The results presented in this Chapter will then lead to the construction of the prototype tomographic system, which will be discussed in detail in a separate Chapter (Chapter 4).

3.1 Time-Resolved Optical Imaging and Early Arriving Photons

Biomedical optical imaging has been explored as an important non-invasive diagnostic technique for detection of tissue abnormalities [Chance & Alfano, 1995; Alfano & Fujimoto, 1996]. At long visible wavelengths and in the near infrared, light can

penetrate deeply into biological tissue, with minimal absorption [Chance & Yodh, 1995]. However, light traversing biological tissue undergoes multiple elastic scattering events. The objective of time-resolved photon migration studies is to reduce or eliminate the resulting turbidity, which obscures small embedded lesions.

Two main experimental approaches have been followed. The first exploits the use of diffusive photons which have undergone multiple scattering events in the media [Patterson et al, 1989; Sevick & Chance, 1991; O'Leary et al, 1992; Boas et al, 1993; Svaasand et al, 1993; Graber et al, 1994; O'Leary et al, 1995; Jiang et al, 1995]. By placing source(s) and detector(s) at various locations, information about he spatial distribution of embedded inhomogeneities can be obtained. The diffusive photons are well modeled by the diffusion theory. By solving the inverse problem numerically, if not analytically, a three dimensional image can, in principle, be reconstructed. Another advantage of this approach is the large signal level. Experimentally, the diffusive photons are usually measured in the frequency domain by amplitude modulation and demodulation of the light source and the detector. In particular, Chance and coworkers have introduced the concept of diffusive photon density waves to obtain spatial information about the embedded inhomogeneities in turbid media. This is based on the observations that phase coherence is maintained in highly turbid media over distances of more than 10 cm, and that these waves, like optical waves, exhibit the Snell, Helmholz and Kirkhoff relationships [O'Leary et al, 1992; Knuttel et al, 1992]. The modulation frequency currently used in this kind of studies is typically 200 MHz. The experimental system using frequency modulation can be very inexpensive. However, because of the

technical difficulties in higher-frequency modulation/demodulation (currently the limit is about 1 GHz), the spatial resolution that can be achieved is expected to be poor due to the broad spatial distribution of the diffusive photons inside the turbid media. Partially due to the lack of analytical solutions to the inverse problem, spatial resolution has not been carefully studied. Therefore this approach, in general, is most useful in detecting large lesions and global optical properties of the tissue, such as stroke and brain hypoxia [Chance, 1992; Fantini et al, 1995].

The second approach uses a forward scattering "transillumination" geometry and exploits the use of the earliest arriving photons, which undergo little or no scattering and traverse the medium in nearly straight-line paths. In principle one can then obtain diffraction-limited spatial resolution in scattering media. Alfano and coworkers [Wang et al, 1991] introduced the term of "ballistic photons" to describe these zero-scattered photons. A variety of techniques have been explored to study this regime. Picosecond time gating techniques, such as those using the Kerr effect [Wang et al, 1993], and ultrafast optical detection [Berg et al, 1993], are commonly used. In addition, these photons can also be detected by their preserved coherent properties, pioneered by Fujimoto and coworkers [Huang et al, 1991]. Various coherent techniques, such as interferometry [Hee et al, 1993] and holography [Hyde et al, 1996], and non-linear optical methods such as stimulated Raman scattering [Bashkansky et al, 1994], have been widely studied. Detection at the very low light intensities which characterize this regime is achieved by coherent/non-linear-optics amplifications. Another advantage of the coherent (i.e., correlation gating) techniques is that, in principle, they do not require

ultrashot laser pulses. Rather, even a CW source with broad bandwidth can be used, since the length of the gate is determined by the coherence time of the laser. Technically, this allows for low-cost systems with high reliabilities. Moreover, because most of these prompt photons traverse the media without being scattered, thus via straight-line paths, high spatial resolution can be obtained. Typically, a shadow image is obtained by 2-D scanning of the source-detector pair, and 3-D information can be reconstructed by acquiring a number of 2-D shadow images through different observation angles [Hebden & Wong, 1993]. However, because of the high degree of scattering in biological tissue, the amount of these earliest arriving photons is very small. In fact, they are basically non-detectable after traversing a couple of centimeter of biological tissues. For example, considering the typical tissue parameters $\mu_s = 10$ mm^{-1} and g = 0.9, the zero-scattering transmission signal through a 1 cm thick piece of tissue is $e^{-100} = 10^{-43}$ of the incident light! Thus, this concept works best in relatively thin samples, such as microscopy specimens [Izatt et al, 1994], or special tissue types that have very small scattering, such as cornea [Huang et al, 1991].

Recently, attention has been directed to the intermediate regime [Benaron & Stevenson, 1993; Mitic et al, 1994], which may provide the best trade-off between the signal-to-noise ratio (S/N) and the spatial resolution. These photons are minimally scattered, thus travel a near straight (or more generally speaking, a well-defined) path. However, in contrast to the ballistic regime, these photons offer detectable signal levels after penetrating thick tissue (several cm). Currently, this regime can only be studied by high resolution time-resolved detection, such as a PMT-based time-resolved single-

photon-counting device or a streak camera; whereas neither frequency (due to the low modulation/demodulation frequency) nor coherent/non-linear-optics techniques (due to the incoherence of the multiple scattered photons) can be used in detect these photons. It has been shown that the spatial resolution achievable critically depends on the time window used [Moon & Reintjes, 1994]. Few-millimeter resolution has been demonstrated in reasonably thick samples (2-4 cm) by using early arriving (up to tens of picoseconds) photons [Benaron & Stevenson, 1993; Mitic et al, 1994]. However, most of these studies do not employ theoretical modeling or inverse algorithm. It is expected that the extraction of the spatial information can be improved by using a theoretical model for these early arriving photons, such as the path integral method [Perelman et al, 1994] or diffusion theory, if applicable [Wu et al, 1995].

3.2 Fluorescence for Contrast

Most photon migration schemes employ differences in absorption/scattering between the embedded objects and the surrounding medium for contrast [Chance & Alfano, 1995; Alfano & Fujimoto, 1996]. However, in many clinical applications, such contrast is usually small. In addition, any changes in intensity are overwhelmed by the huge excitation background. Alternatively, fluorescence can also be used to provide contrast. Fluorescence spectroscopy studies have suggested that endogenous tissue fluorophores may provide useful diagnostic information [Campbell & Dwek, 1984]. In addition, selective uptake of many exogenous dyes (1 to 100 μM concentration [Nishiwaki et al, 1989]), such as those used in photodynamic therapy (PDT) [Johansson,

1993], has been demonstrated in neoplastic lesions. This selective uptake is able to provide contrast ratio between 2:1 to 80:1 depending on tissue type [Johansson, 1993]. Several mechanisms have been suggested to explain this selective uptake, including increased vasculature in the tumor mass, increased permeability in the blood vessel walls, increased metabolic rate in tumor cells, etc. Generally speaking, a 10:1 contrast ratio is believed achievable in breast tumor detection [Private communication with Dr. Oseroff]. More recently, fluorescence labeled tumor specific antibodies have been suggested to provide much better selectivity, thus contrast ratio (> 100:1) and reasonable concentration levels (about 0.1 μM range) [Chance, 1995]. The antigen-antibody interaction is highly specific, and various types of tumors are known to express tumor-specific antigens on the cell surfaces due to the underlying genetic changes in the tumor cell growth [Abbas *et al*, 1994]. In addition, high quantum yield fluorophore molecules can be linked to the antibody to provide a spectroscopic label to differentiate the tumor cells from their normal surroundings [Tsien & Waggoner, 1995]. Therefore, both PDT agents and fluorescence-labeled antibodies can serve as fluorescent markers with high quantum yields to locate embedded tumors. Besides enhanced contrast, the use of fluorescence avoids the interference from the excitation light and provides biochemical information for diagnosis (either direct information from the native fluorophores or indirect information from the contrast agents, depending upon the exact mechanisms of accumulation in the targets). However, the use of fluorescence has been limited by the concern that the long fluorescent lifetimes, typically of the order of a few nanoseconds [Campbell & Dwek, 1984], inevitably obscures the desired temporal resolution.

In the following sections of this chapter, we will show first that the long fluorescence lifetime does not affect temporal resolution, provided that the very early part of the observed signal is used to extract the spatial information. Then initial experimental studies will be presented to image embedded fluorescent objects using early arriving fluorescence photons.

3.3 Temporal Resolution of the Early Arriving Fluorescence Photons

Generally speaking, the time evolution of the observed signal from the fluorescent objects embedded in turbid media is determined by both the time-course of the photon migration through the media and the decaying fluorescence. The excitation photon from an incident laser pulse propagates through the medium to reach the embedded fluorophore. Then, the excitation photon is absorbed and after a certain time delay, described by the fluorescence lifetime, an emission photon is generated. The emitted fluorescence photon again migrates through the medium until being detected. Mathematically, the observed signal can be written as the temporal convolution of the three processes. Note that because the electronic excitation from the ground state to the excited state is extremely rapid, on the order of 10^{-13} second [Campbell & Dwek, 1984], the rising edge of the fluorescence lifetime curve is effectively a step function. Thus, in the observed time-resolved fluorescence signal, the early part is mainly determined by that of the photon migration, while the long fluorescence decay time, on the order of nanoseconds, only affects the later part of the curve.

In order to experimentally validate that fluorescence can be used to provide time-of-flight signals for ranging, despite the long fluorescence lifetimes relative to the photon migration time of interest, a simple, single-ended experiment was performed using picosecond pulses for excitation and time-resolved single-photon counting for detection, Fig. 3.1. In this experiment, the 1064 nm laser light from a mode-locked Nd:YAG laser (Coherent Antares 76) is frequency doubled (CSK Superdoubler) and used to pump a dye laser (Coherent 599) coupled to a cavity dumper (Coherent 7220). The laser wavelength is 570 nm, pulse duration less than 10 ps, the repetition rate 1 MHz and the average power 30 mW. The backscattered signal is collected by a 400 μm core optical fiber positioned adjacent to the incident beam on the same surface of the turbid media, and
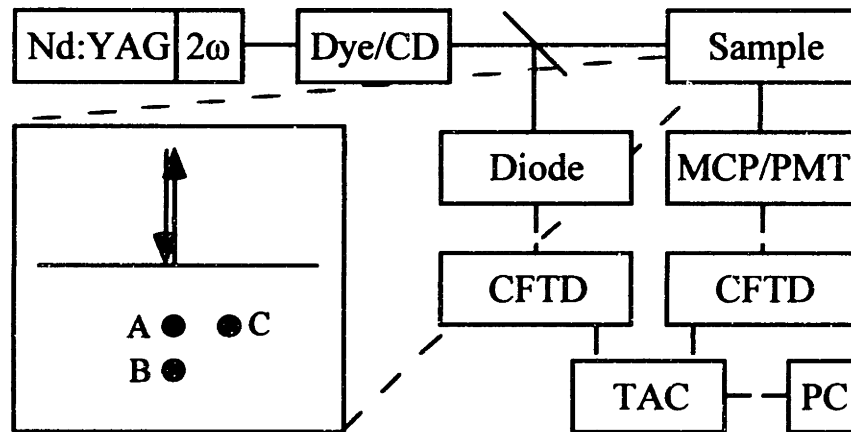

Figure 3.1. Schematic diagram showing instrument components used in this study. CD: cavity dumper; MCP/PMT: microchannel plate/photomultiplier tube; CFTD: constant fraction time discriminator; TAC: time-to-amplitude converter. Solid lines represent optic signal and dashed electronic signal. The insert shows the arrangement of excitation and collection probes, and the sample geometry.

delivered to a photomultiplier tube (PMT, Hamamatsu R1564U-01). The signal from the PMT is fed to a time-to-amplitude converter (Canberra 2145) and then transferred to a microcomputer for later analysis. A 10 nm band pass filter (centered at 610 nm) and a 600 nm long pass filter in front of the detector completely remove the excitation light. The temporal resolution of this system is mainly determined by the PMT transition time spread, which is about 70 ps.

Suspensions of 1 μm diameter polystyrene spheres purchased from PolySciences (Warrington, PA) were used as scatterers. The scattering properties of the polystyrene beads were evaluated by the standard Mie theory calculation [Bohran & Huffman, 1983]. Given the refractive index of the medium (water, n=1.33) and the scattering particles (polystyrene beads, n=1.59), the particle size and the optical wavelength, the scattering cross-section and anisotropy (g) coefficients for individual scattering particles were calculated. The scattering coefficient (μ_s) was then obtained as the product of the single-particle cross-section and the particle density. Rhodamine 6G (R6G) and rose bengal (RB) were purchased from Exciton (Dayton, OH) and Aldrich Chemicals (Milwaukee, WI) and were dissolved at approximately 2 mM concentration in methanol and water respectively. Glass spherical cells of 1 cm diameter containing the fluorescence dyes were positioned at various depths below the surface as the embedded objects.

Time-resolved fluorescence signals were obtained from dye cells containing either RB (130 ps lifetime in water) or R6G (3.9 ns lifetime) embedded in a polystyrene suspension at different depths. The results are plotted in Figs. 3.2(a) and (b). In spite of the fact that the fluorescence lifetimes of RB and R6G differ by a factor of 30, the rising
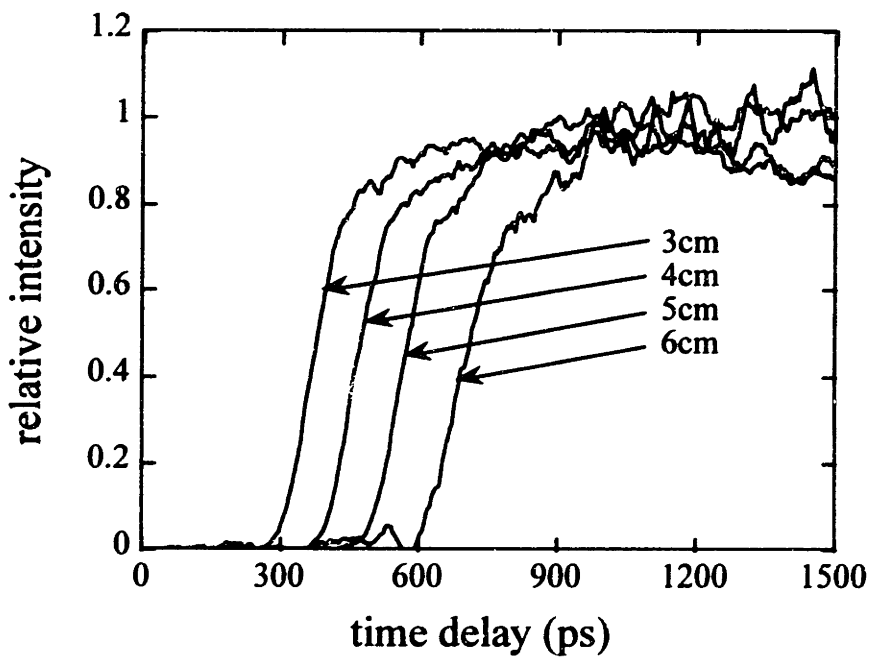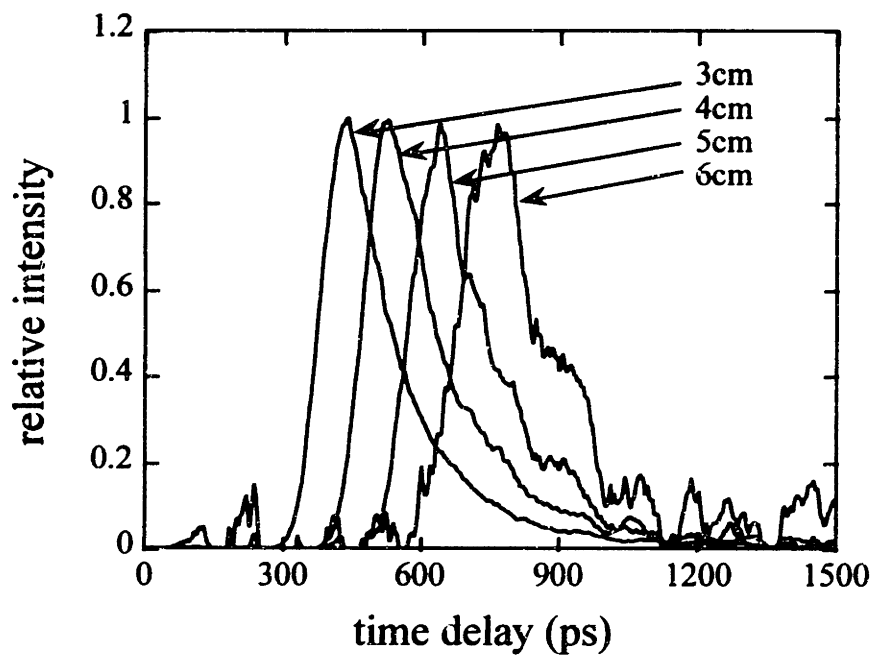
Figure 3.2. Experimental results with fluorescence emission from RB (a) and R6G (b)

dye cell embedded at different depths below the surface.

edges of these two curves are extremely similar. In fact, they closely represent the rising edges of the photon migration curves. Thus, it is demonstrated that the early arriving fluorescence emission can be used as a probe to provide accurate timing information, despite the long fluorescence decay time. Therefore, it should be able to provide high resolution spatial information about the fluorescent objects embedded in a turbid medium.

3.4 Single Probe Imaging Studies

After it was demonstrated that the early arriving fluorescence photons can be used to provide accurate temporal information, additional experiments were performed with a similar setup to image embedded fluorescent objects. In this single-ended geometry the earliest arriving fluorescence photons emitted from the closest object (A) should return to the collection fiber sooner than those from object B, located at a greater depth, or object C, laterally displaced from A (inset, Fig. 3.1). Thus, this simple arrangement allows us to probe the location of the fluorescent object in three dimensions by observing the time-resolved fluorescence signal. In addition, ultrafast time-gating can be used to further improve the spatial resolution.

Rhodamine 6G (R6G, sulforhodamine 640 (S640), hexacyanine 2 (HIDCI) and β-carotene were purchased from Exciton and Aldrich Chemicals. The fluorescence dye concentrations for R6G, S640 and HIDCI were approximately 2 mM in ethylene glycol, methanol and methanol, respectively. Again, suspensions of 1 μm diameter polystyrene

spheres purchased from PolySciences were used as scatterers and glass spherical cells of 1 cm diameter containing various dyes are used as the embedded objects.

Depth of a Fluorescent Object

Time-resolved fluorescence signals were obtained from a fluorescent object containing R6G solution embedded at different depths inside the medium. As shown in Fig. 3.2, the depth information can be easily probed in the backscattering geometry by looking at the earliest-arriving fluorescence photons. The time-of-flight for these earliest arriving photons is proportional to twice the depth of the fluorescent object. As expected, fluorescence emitted from a deeper object arrives at the detector later. In addition, increased scattering also delays the arrival time, as shown in the plot of depths vs. time, Fig. 3.3. Here we use the time at which the signal reaches half maximum, $t_{1/2}$, as the representative time for each curve.
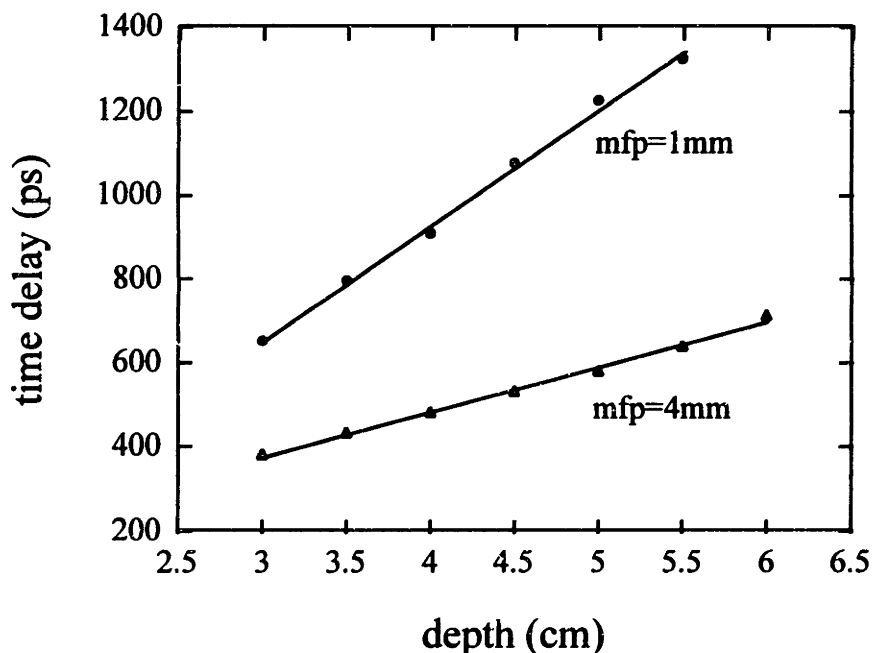

Figure 3.3. Depths of a fluorophore vs. $t_{1/2}$ for two different scattering coefficients.

Lateral Location of a Fluorescent Object

To obtain lateral information about an embedded object, the time-resolved fluorescence signals were measured as a function of the lateral position of the R6G dye cell at the depth of 5 cm. Based on simple geometrical considerations, we expect the lateral resolution to be poorer than the depth resolution. However, lateral resolution can be improved by using an ultrafast time window for the earliest arriving photons, which is similar to the typical time-gating transillumination imaging experiments. The optimum time gate was chosen based on considerations of both resolution and S/N ratio. Typically, a 24 ps time window was used in this study. Figure 3.4 plots the time gated intensity vs. the lateral displacement of the fluorescence dye cell at 25 and 100 scattering mean free paths (mfp), respectively. A lateral resolution of 1 cm is obtained with this time
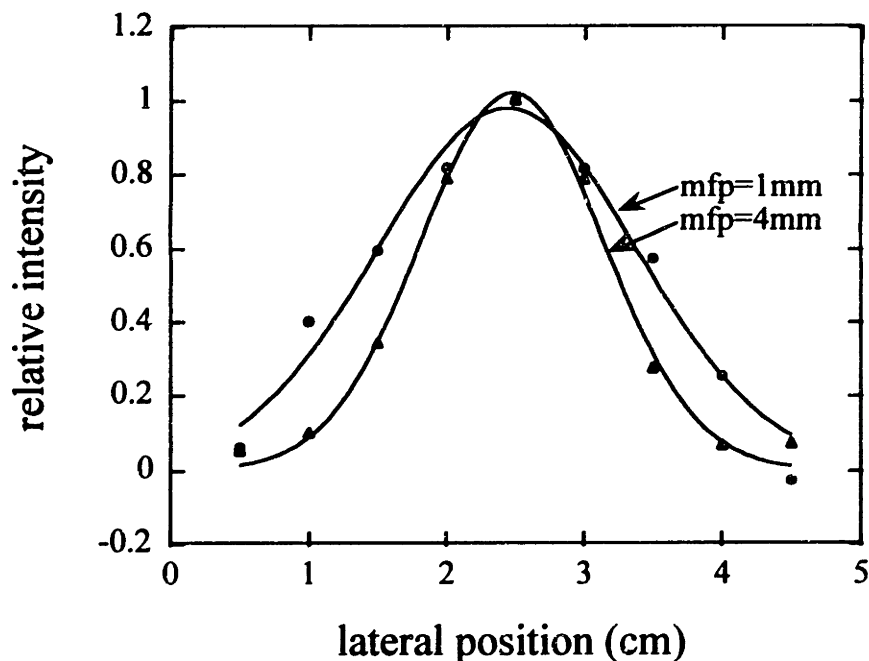

Figure 3.4. Lateral location of a fluorophore using ultrafast time-gating for two different scattering coefficients.

window.

In summary, the above experiments show that the early portions of the fluorescence signals can be used to image embedded objects in turbid media. The earliest signals observed in this case are proportional to twice the distance from the sample surface to the location of the embedded objects. Thus, the arrival time of the earliest photons can provide the depth information of the embedded objects (Figs. 3.2 and 3.3), as well as the usual 2-D localization (Fig. 3.4). In addition, lateral spatial resolution can be optimized by using a short duration time-gate to select the earliest arriving photons.

Multiple Objects

Experiments were also conducted with two embedded cells containing the same fluorescence dye, R6G. The two objects were positioned 1.8 cm apart at depths of 4.5 and 5 cm, respectively. Using lateral displacement and time delay as variables, we constructed a contour map of the time-derivative of the time-resolved intensity (Fig. 3.5). The time-derivative, a measure of how fast the time-resolved signal evolves, reaches a maximum at approximately $t_{1/2}$, which in turn provides the depth information (Fig. 3.3). As can be seen, although the signal from the shallower object dominated, the 3-D positions of both objects could be ascertained. This is because we can use different time-gating to probe different depth inside the turbid media. This result clearly demonstrates the feasibility and potential of this spectral, tomographic technique by the use of early arriving fluorescence photons. Note that although the lateral dimension represents the actual image of the object, longitudinally (i.e., temporally) it only provides information

about the top surface of the fluorescent objects. Also note that the best lateral resolution is obtained at the earliest time gate, i.e. where the contours begin along the time axis.
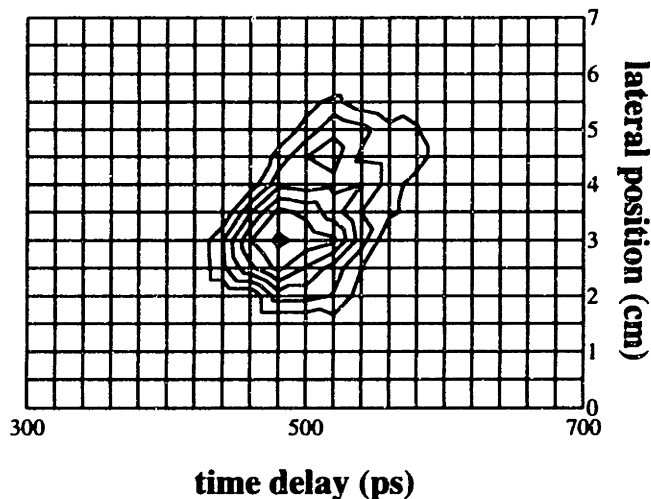
Figure 3.5.   Probing two identical fluorophores at different depths.

If the two embedded objects have distinct spectroscopic features, imaging capability can be remarkably enhanced. This was demonstrated by measuring the fluorescence intensity from two cells (similar geometry as in Fig. 3.5) containing S640 and HIDCI at 620 and 670 nm, respectively, (Fig. 3.6) by placing a spectrometer in front of the PMT. Compared to Fig. 3.5, signal interference between the two objects is dramatically reduced, and more importantly, the chemical identities of the objects can be obtained.
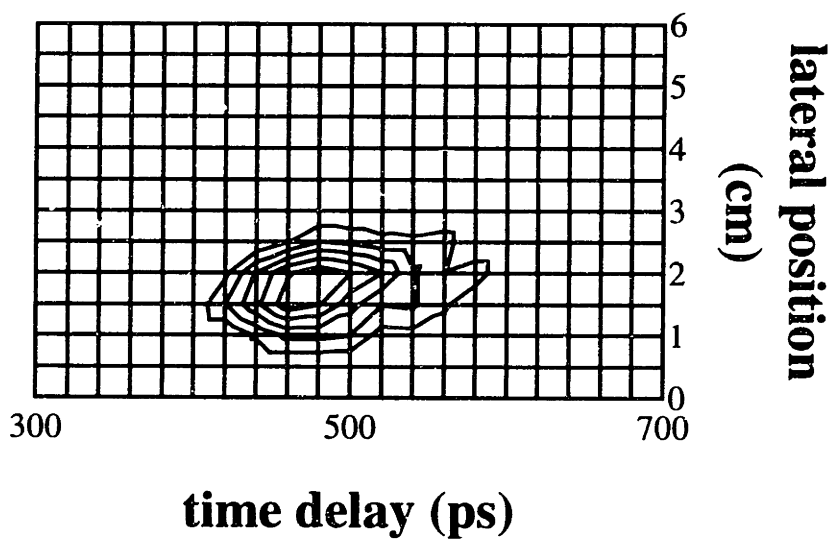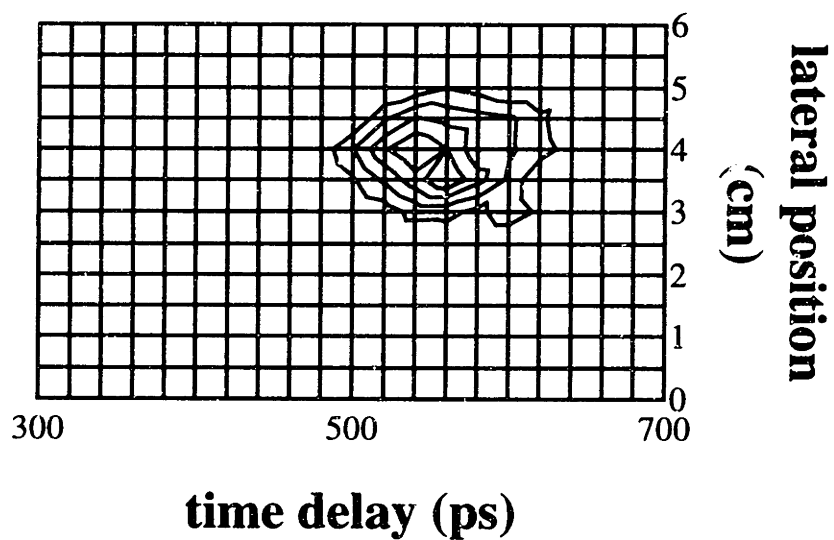
Figure 3.6. Probing two different fluorophores detected at 620 nm (a) and 670 nm (b).

Raman Scattering

In addition to fluorescence, the instantaneous Raman scattering can also be used to provide accurate timing information. In this experiment, a Raman scattering cellcontaining β-carotene (Aldrich Chemicals, 4 mM in benzene) was embedded in the turbid medium. With 570 nm excitation and a 10 nm bandpass filter centered at 610 nm, the pre-resonance enhanced Raman scattering from the β-carotene vibration at 1157 cm^{-1} was studied. To validate that the detected signals are from Raman scattering rather than fluorescence from either β-carotene or sample impurities, we checked that without the scattering medium the time-resolved Raman scattering was identical in shape to that of the laser light (determined by instrumental resolution), obtained by deflecting part of the laser beam into the fiber probe and removing the filters. This is consistent with the

Figure 3.7. Experimental results with Raman scattering from β-carotene cell at three depths.

instantaneous nature of Raman scattering. The possibility of laser light leakage was excluded by replacing the Raman cell with a Raleigh scattering cell containing KI pow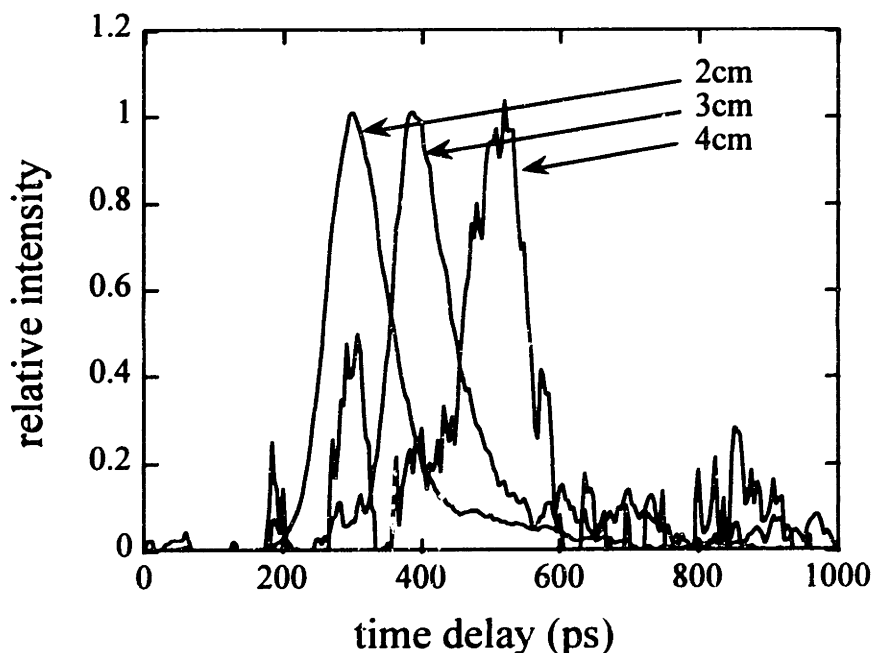der, which does not have Raman bands above 300 cm^{-1}. As a further check, the emission spectrum from the Raman sample was collected using a Spex Fluorolog spectrofluorimeter with the same 570 nm excitation. Distinct Raman peaks at 605, 610 and 624 nm, which correspond to the known [Rimai et al, 1970] Raman shifts of 1008, 1157 and 1516 cm^{-1} for β-carotene, were observed with minimum background. Figure 3.7 displays the time-resolved Raman signal for cell depths of 2, 3 and 4 cm in a scattering medium with 7 mm mfp. This experiment demonstrates the feasibility of using Raman scattering, as well as fluorescence, as a spectroscopic indicator.

3.5 Conclusions

This chapter presented initial studies of using time-resolved spectroscopic techniques to detect fluorescent objects embedded in turbid media. Early arriving fluorescence photons are used to provide the optimal trade-off between the S/N and the temporal resolution with enhanced contrast. In addition, it is shown that the early arriving fluorescence photons are not sensitive to the long fluorescence lifetime, thus providing accurate timing information. Time gating and spatial probing are combined to detect multiple objects. The locations of objects at the same depth can be obtained by lateral scanning, and the resolution can be enhanced by selecting the optimal delay and interval for time-resolved measurement. When the objects are located at different depths, time-gating can provide additional information about the distances of those objects from

the surface. The results of Figs. 3.2-3.5 demonstrate that high resolution, 3-D spatial information of the hidden objects can be obtained from fluorescence emission. Lastly, Fig. 3.6 demonstrates the feasibility of distinguishing objects utilizing their different spectroscopic features.

References

A. Abbas, A. Litchman, & J. Pober, 1994, Cellular and Molecular Immunology, 2nd ed., (W.B.Saunders Company, Philadelphia).

R. Alfano & J. Fujimoto, 1996, Advances in Optical Imaging and Photon Migration TOPS-96, (OSA, Orlando).

M. Bashkansky, C. Adler, & J. Reintjes, 1994, "Coherently amplified Raman polarization gate for imaging through scattering materials," Opt. Lett., pp 350.

D. Benaron & D. Stevenson, 1993, "Optical time-of-flight and absorbance imaging of biologic media," Science, pp 1463.

R. Berg, O. Jarlman, S. Svanberg, 1993, "Medical transillumination imaging using short-pulse diode lasers", Appl. Opt., pp 574.

D. Boas, M. O'Leary, B. Chance, & A. Yodh, 1993, "Scattering and wavelength transduction of diffuse photon density waves," Phys. Rev. E, pp R2999.

C. Bohren & D. Huffman, 1983, Absorption and Scattering of Light by Small Particles, (Wiley, New York).

I. Campbell & R. Dwek, 1984, Biological Spectroscopy, (Benjamin/Cummings Publishing, Menlo Park).

B. Chance & R. Alfano, 1995, Proceedings of Optical Tomography, Photon Migration, and Spectroscopy of Tissue and Model Media: Theory, Human Studies, and Instrumentation, SPIE 2389.

B. Chance, 1992 "Early detection of brain ischemia and hemorrhage by optical methods," SPIE 1641, pp 163.

B. Chance, 1995, "Time-resolved spectroscopy and imaging," SPIE 2389, pp 122.

S. Fantini, M. Franceschini, J. Maier, S. Walker, B. Barbieri, & E. Gratton, 1995, "Frequency-domain multichannel optical detector for non-invasive tissue spectroscopy and oximetry," Opt. Eng., pp 32.

H. Graber, J. Chang, R. Barbour, & R. Aronson, 1994, "Evaluation of spatial variations in the time and frequency dependence of imaging operators for diffusion tomography," in Advances In Photon Migration Imaging And Optical Tomography, Orlando, pp 95.

J. Hebden & K. Wong, 1993, "Time-resolved optical tomography," Appl. Opt., pp 372.

M. Hee, J. Izatt, J. Jacobson, J. Fujimoto, E. Swanson, 1993, "Femtosecond transillumination optical coherence tomography," Opt. Lett., pp 950.

D. Huang, E. Swanson, C. Lin, J. Schuman, W. Stingson, W. Chang, M. Hee, T. Flotte, K. Gregory, C. Puliafito, & J. Fujimoto, 1991, "Optical coherence tomography," Science, pp 1178.

S. Hyde, N. Barry, R. Jones, J. Dainty, & P. French, 1996 "High resolution depth resolved imaging through scattering media using time-resolved holography," Optics Comm., to be published.

J. Izatt, M. Hee, G. Owen, E. Swanson, & J. Fujimoto, 1994, "Optical coherent microscopy in scattering media," Opt. Lett., pp 590.

H. Jiang, K. Paulsen, U. Osterberg, B. Pogue, & M. Patterson, 1995, "Simultaneous reconstruction of absorption and scattering profiles in turbid media from near-infrared frequency-domain data," Opt. Lett., pp 2128.

J. Johansson, 1993, *Fluorescence Spectroscopy for Medical and Environmental Diagnostics*, Ph.D. thesis, Lund Institute of Technology, Lund, Sweden.

A. Knuttel, J. Schmitt, & R. Knutson, 1992, "Spatial localization of absorbing bodies by interfering diffusive photon density waves," *Appl. Opt.*, pp 381.

J. Moon & J. Reintjes, 1994, "Image resolution by use of multiple scattered light," Opt. Lett., pp 521.

Y. Nishiwaki, S. Nakamara, & S. Sakaguchi, 1989, "New method of photosensitizer accumulation for photodynamic therapy in an experimental liver tumor," *Lasers Surg. Med.*, pp 254.

M. O'Leary, D. Boas, B. Chance, & A. Yodh, 1992, "Refraction of diffusion photon density waves," Phys. Rev. Lett., pp 2658.

M. O'Leary, D. Boas, B. Chance, & A. Yodh, 1994, "Reradiation and imaging of diffuse photon density waves using fluorescent inhomogeneities," J. Luminescence, pp 281.

M. O'Leary, D. Boas, B. Chance, & A. Yodh, 1995, "Experimental images of heterogeneous turbid media by frequency-domain diffusing photon tomography," Opt. Lett., pp 426.

M. Patterson, B. Chance, & B. Wilson, 1989, "Time resolved reflectance and transmittance for the noninvasive measurement of tissue optical properties," Appl. Opt., pp 2331.

L. Perelman, J. Wu, I. Itzkan, & M. Feld, 1994, "Photon migration in turbid media using path integrals," Phys. Rev. Lett., pp 1341.

L. Perelman, J. Wu, I. Itzkan, Y. Wang, R. Dasari, & M. Feld, 1995, "Time-dependent photon migration using path integrals," Phys. Rev. E, pp 6134.

L. Rimai, R. Kilporen, & D. Gill, 1970, "Excitation profiles of laser Raman spectra in the resonance regions of two carotenoid pigments in solutions," J. Am. Chem. Soc., pp 3824.

E. Sevick & B. Chance, 1991, "Photon migration in a model of the head measured using time- and frequency- domain techniques: potentials of spectroscopy and imaging," Proc. SPIE 1431, pp 84.

L. Svaasand, B. Tromberg, R. Haskell, T. Tsay, & M. Berns, 1993, "Tissue characterization and imaging using photon density waves," Opt. Eng., pp 258.

R. Tsien & A. Waggoner, 1995, Handbook of Biological Confocal Microscopy, 2nd ed., Chapter 16, (Plenum Press, New York).

L. Wang, P. Ho, C. Liu, G. Zhang, & R. Alfano, 1991, "Ballistic 2-D imaging through scattering walls using an ultrafast Kerr gate," Science, pp 769.

L. Wang, P. Ho, & R. Alfano, 1993, "Double-stage picosecond Kerr gate for ballistic time-gated optical imaging in turbid media," Appl. Opt., pp 535.

Chapter 4

Prototype Tomographic Imaging System

The last Chapter presented some preliminary experimental results of using early arriving photons to detect embedded fluorescent objects in a turbid medium. In this Chapter, we will advance this approach and describe a prototype tomographic system using early arriving fluorescence photons. It consists of a state-of-the-art picosecond laser system and a streak camera. Phantom experiments using typical tissue optical parameters and a cylindrical geometry similar in size to a human breast are performed. A Laplace transform based inverse algorithm is developed to analyze the multichannel time-resolved data, which provides accurate estimation in localizing and resolving embedded objects. This algorithm also correctly treats the tissue-air boundary effect based on the convolution picture presented in Chapter Two. Lastly, the S/N of the system is fully characterized so that some clinical projections of this technique can be inferred.

4.1 System Description

This section describes the instrumentation details of our prototype tomographic system to detect embedded fluorescent objects using a multi-channel time-resolved technique. An overview is first presented by following a schematic diagram of the system. Detailed information about the operation of the instrument is incorporated into

the performance analysis Section 4.2, which examines the optical/electronic properties of every individual component in the system.

The schematic diagram of the prototype tomographic experimental apparatus is depicted in Fig. 4.1. It consists of a ~ 2 ps pulsed laser (Coherent Mira 900 mode-locked Ti:sapphire laser pumped by Coherent Innova 400 argon ion laser) for excitation and a streak camera system (Hamamatsu C5680 with M5675 Synchroscan Unit) for detection. The excitation wavelength is 752 nm, the repetition rate is 76 MHz. A small portion of the excitation light is deflected by a quartz plate to a fast photodiode (Hamamatsu C1808-02) as the optical triggering signal, so that the streak camera is synchronized with the laser pulses. Eight coherent fiber bundles (Sumitomo, Ltd.) are used to collect the fluorescence light and transmit it to the streak camera. Each fiber bundle is 500 µm in diameter and consists of ten thousand single-mode silica fibers. This allows maximum optical throughput (ten thousand times the throughput of a single-mode fiber) with minimum temporal dispersion. Two 752 nm holographic notch filters (Kaiser, Inc.) are used to remove the excitation light. A 725 nm long pass filter is also utilized to remove any stray light in the room. Fluorescence emission from 765 to 800 nm is detected by the streak camera. The temporal calibration of the streak camera is performed by setting up an optical delay line using a retroreflector on a translation stage. The CCD response of the streak camera is also calibrated by simply allowing the room light (spatially diffused and temporally constant) to enter the camera. The streak camera can be operated either in the "digital" mode or the "analog" mode (see below). In this thesis research, digital mode operation is usually used except in the background fluorescence studies, Section 4.5. In

addition, the streak camera can be operated at different sweep speeds which offer

different temporal resolutions and window widths: speed one offers the best temporal

resolution of 2 ps; whereas speed four offers the widest time window of 1.5 ns. All the

current studies use sweep speed four in data collection. Under these conditions, the best

temporal resolution of the system is about 10 ps, which includes the laser pulse duration,

the temporal dispersion through a 5 foot length of the fiber bundles, and the streak camera

temporal resolution, optimized by closing the entrance slit width to < 10 μm. However,

in all the experiments reported in this thesis, the system temporal resolution is mainly

determined by the height of the streak camera photocathode, 150 μm, by widely opening

the input slit. This ensures the maximal S/N level with reasonably good temporal

resolution (~50 ps).

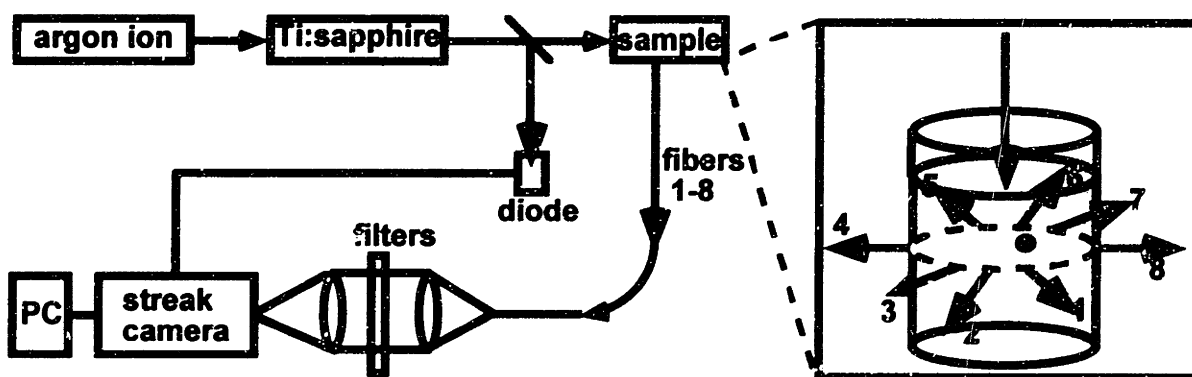Figure 4.1. Schematic diagram of experimental apparatus and sample geometry.

The phantom sample is contained in a cylindrical glass beaker 6.4 cm diameter.

The excitation beam impinges perpendicularly on the sample at the center of the top

surface. The distal ends of the eight detection fiber bundles are evenly positioned around

the circumference of the beaker in the horizontal plane containing the embedded

fluorescent objects. The depth of this plane is about 1.5 cm below the top surface. The proximal ends of the fiber bundles are arranged in a line and imaged onto the streak camera input slit. The streak camera is used as both a time- and a spatially-resolved multichannel detector. Signals from different fiber bundles appear at different horizontal locations on the CCD array of the streak camera, and the temporal information is displayed vertically.

In the first experiment designed to test the system performance, 60 ml of 1 μm diameter 2.5% polystyrene bead stock solution (PolyScience, Inc.) was mixed in 200 ml of water, with black ink (Haggins, Inc., Newark, NJ) added as the turbid medium. This mixture was designed to match the optical parameters of human breast tissue [Mitic *et al*, 1994]. Using Mie theory [Bohren & Huffman, 1983], we calculated, using the method detailed in Chapter 3, that in the wavelength range from 750 to 800 nm the scattering coefficient, μ_s, of the medium ranges from 144 to 160 cm^{-1} (thus the diameter of the beaker is equal to about 1000 scattering mean free paths); and the anisotropy coefficient, g, is between 0.954 and 0.959. Thus the reduced scattering coefficient, μ_s', defined as $\mu_s(1-g)$, varies between 6.88 and 6.96 cm^{-1}. Black ink, whose absorbance was measured using a Shimadzu UV-265 spectrophotometer, was added so that the absorption coefficient, μ_a, was about 0.05 cm^{-1}. The embedded fluorescent objects were 1 mm glass cells filled with 65 μM HITCI dye (Exciton, Inc.) dissolved in methanol. Figure 4.2 shows typical streak camera measurements under the conditions of 600 mW laser power, 1 minute data accumulation time, and the digital mode operation of the CCD. The full temporal window is about 1.5 ns, which is significantly shorter than the signal duration.

In the experiment, the time delay was adjusted so that the very early arriving fluorescence photons were measured. In Fig. 4.2(a), the fluorophore was positioned at the center of the beaker, therefore the eight collection channels receive roughly the same amount of signal. In Fig. 4.2(b), the fluorophore was displaced 1 mm from the center, and as expected, one of the fiber receives the signal earlier than others. Apparently, this preliminary data demonstrates that the prototype tomographic system is able to detect deeply embedded object and that the system is very sensitive to the location of the embedded object.

4.2 Performance Analysis

At this point, it is important to compare the detected signal level with that expected based on the understanding of the physical processes involved in the system, in order to make sure that the system is working properly. This can be estimated by considering the signal response in each individual component of the system. Initially, a certain number of photons,

$$N_0 = \frac{PT}{h\nu} = \frac{0.6 \times 60}{6.63 \times 10^{-34} \times 4 \times 10^{14}} = 1.4 \times 10^{20}, \tag{4.1}$$

enter the system, where P is the incident laser power, 600 mW, T is the data accumulation time, 1 minute, h is the Planck's constant, and ν is the optical frequency (for 750 nm light, ν=4.0x10^{14} sec^{-1}). These photons then migrate inside the phantom medium, which results in a temporal response, determined by the optical parameters of the medium, at the position of the embedded fluorophore, $U_{in}(t)$ (units mm^{-2}ps^{-1}). This time-resolved response can be estimated using the standard solution to the diffusion equation in a semi infinite medium [Patterson et al, 1989]. Here, a semi-infinite medium is a good
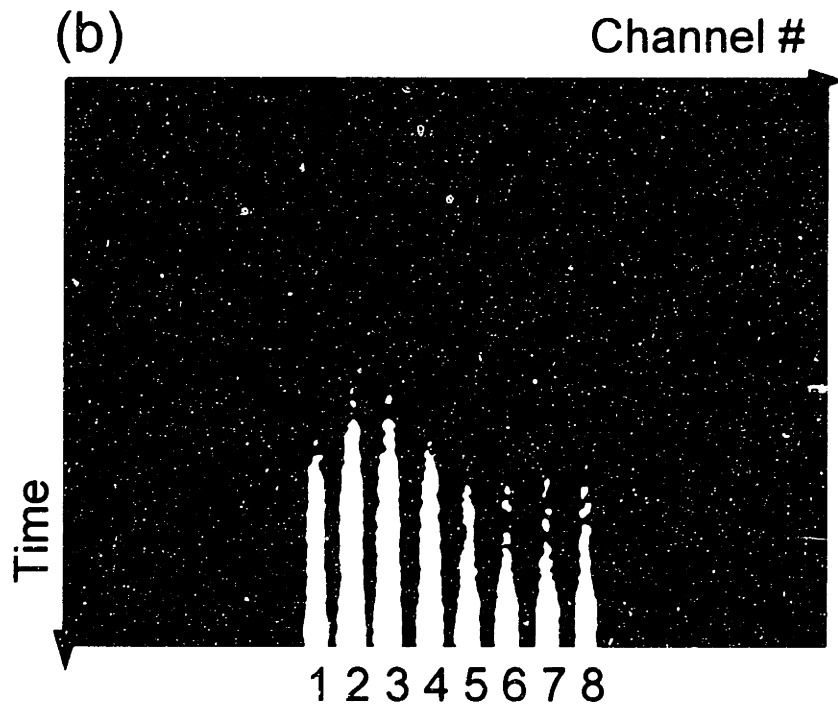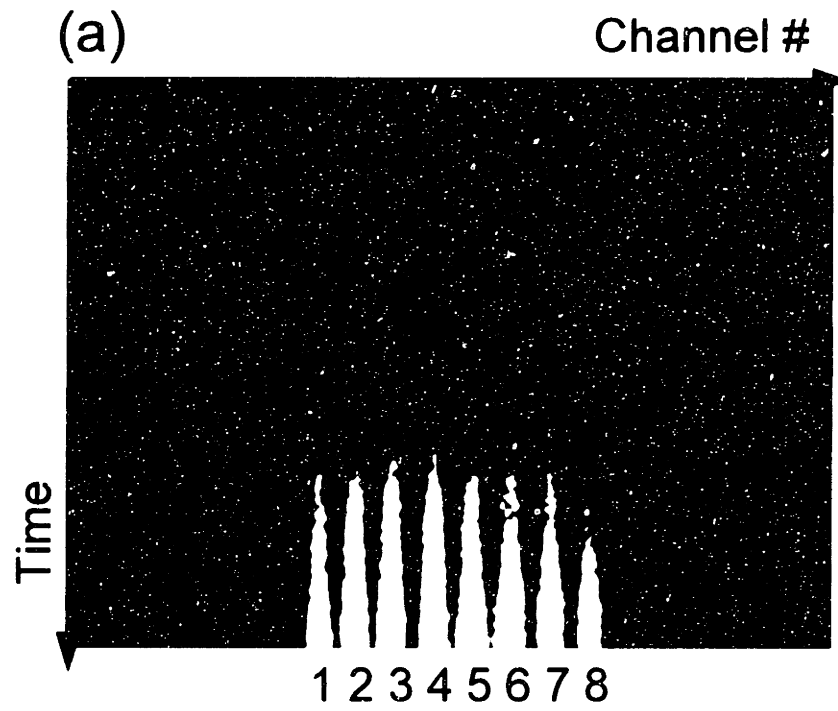
Figure 4.2. Streak camera data: (a) the object is at the center of the beaker. and (b) the object is 1 mm away from the center.

approximation for the beaker geometry since the curvature of the beaker (32 mm) is much

bigger than the transport mean free path (~1 mm). Note in this approximation, the index-

mismatch at the boundary is not included. However, as discussed in Chapter 2, the effect

of the index-mismatch at the boundary can be modeled by an extra convolution term,

which will be discussed below. Thus:

$$U_{in}(t) = (4\pi Dc)^{-3/2} z_0 t^{-5/2} \exp(-\frac{\rho^2 + z_0^2}{4Dct} - \mu_a ct) \tag{4.2}$$

where z_0 is the depth of the fluorophore, and ρ is its radial displacement from the axis of

the incident beam. Note that in fact, Eq. 4.2 was derived [Patterson *et al*, 1989] for the

net flow of photons out of the surface due to an isotropic emission source embedded at

$z=z_0$. Here, we use this equation to calculate the photon number reaching the point $z=z_0$

when there is a net photon flow into the medium from the surface. Physically, these two
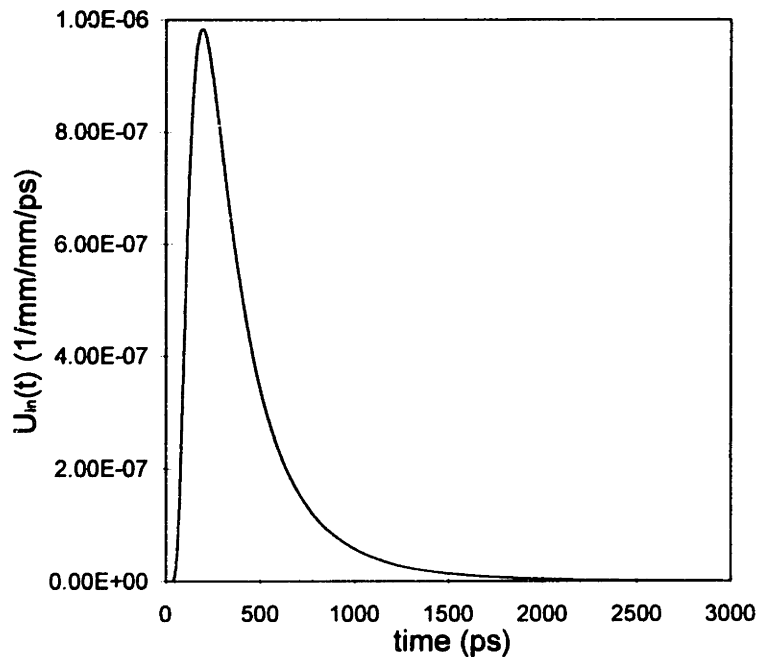

Figure 4.3. Diffusion solution of $U_{in}(t)$ using Eq. 4.2.

picture are related as time-reversed processes and thus they should be equivalent. However, mathematically, in the forward situation, it is necessary to introduce a light source very close to the boundary [Patterson et al, 1989], a situation poorly handled by the diffusion approximation. On the other hand, in the backward situation, the source is always far away from the boundary, thus the diffusion solution works better in this case. When compared with the Monte Carlo simulation, the latter method gives better agreement. The result of Eq. 4.2 is plotted in Fig. 4.3 for $z_0 = 15$ mm and $\rho = 0$ mm.

So far, an index-matched boundary condition has been assumed. As discussed in Chapter 2, the correction due to the index-mismatched boundary condition can be written as an additional convolution term, $G_{b.c.}(t)$ (units ps^{-1}), which can be calculated for a given set of tissue optical parameters, but independent of the position of the original light source, using Monte Carlo simulation, Fig. 4.4. In the Monte Carlo simulation, the
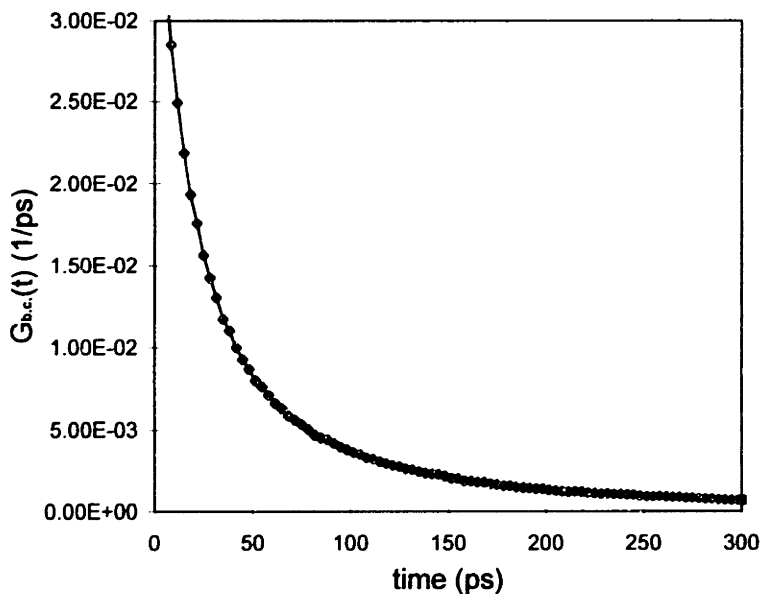

Figure 4.4. Monte Carlo calculation of $G_{b.c.}(t)$.

photons emerging from the index-mismatched surface are calculated for an instantaneous emission source located right under the boundary. The optical parameters of the phantom, μ_a=0.005 mm^{-1}, μ_s'=0.7 mm^{-1} and refractive index-mismatch of 1.33, are used in the simulation.

Next, a certain portion of the incident light is absorbed by the fluorophore located at $z=z_0$. This equals to the intensity multiplied by the volume, a^3, and the absorption coefficient, μ_a, of the embedded object. Note that the absorption coefficient can be written as the product of the fluorophore concentration, C, the absorbance of the molecule, ε, and $ln10$. For HITCI in methanol at 750 nm, we measured, using the Shimadzu UV-265 spectrophotometer, μ_a= 0.07 mm^{-1}μM^{-1} x C. In addition, if the object is optically thick, a certain reduction, r_{thick}, in the absorption rate has to be included (Here, we estimate r_{thick} = $1/\mu_a a$ = 0.22 for a 1 mm object and 65 μM HITCI concentration). Assuming the fluorescence quantum yield is η_f and the lifetime is τ (i.e., the fluorescence decay $F(t) = \dfrac{1}{\tau}\exp(-t/\tau)$), then the fluorescence emission strength (units ps^{-1}) is given by:

$$N_0\{\mu_a a^3 r_{thick}\eta_f\} \times \{U_{in}(t) \otimes G_{b.c.}(t) \otimes F(t)\}. \tag{4.3}$$

For HITCI, η_f = 0.28 for the entire emission wavelength. From 765 to 800 nm, the effective quantum yield is about 0.14 (half of the total η_f) as measured using the Spex Fluorolog spectrofluorimeter. The lifetime of HITCI dissolved in methanol is about 900 ps, as measured by the streak camera.

The fluorescence photons emitted by the fluorophore migrate in the phantom until they reach the collection fibers. This process is again governed by the diffusion process and its response, $U_{out}(t)$ (units $mm^{-2}ps^{-1}$), can be estimated similarly to $U_{in}(t)$ using Eq. 4.2. Figure 4.5 plots the result for $z_0 = 32$ mm and $\rho = 0$ mm, i.e., the fluorophore is at the center of the 64 mm beaker and in the plane of the detection fibers. Again, an extra convolution term has to be included to account for the index-mismatched boundary.
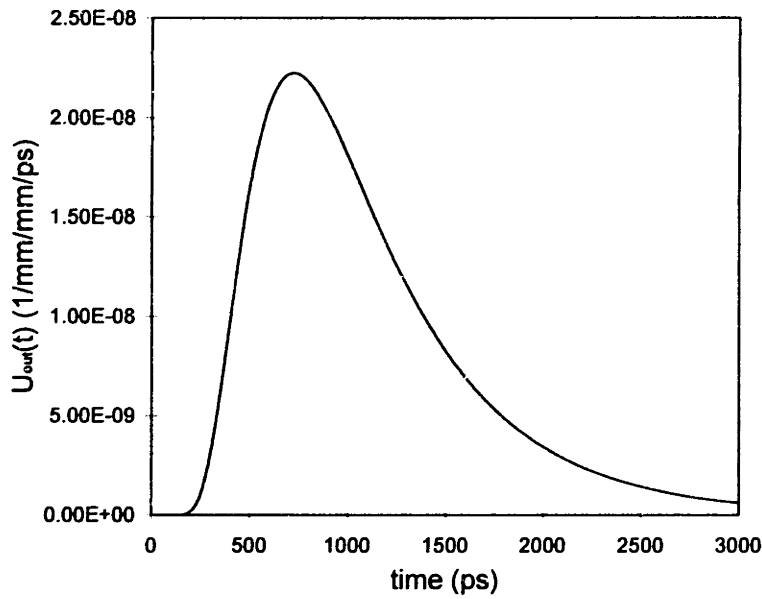

Figure 4.5. Diffusion solution of $U_{out}(t)$ using Eq. 4.2.

Thus the fluorescence photon flux rate at the fiber proximal end (units $mm^{-2}ps^{-1}$) is given by:

$$N_0 \{\mu_a a^3 r_{thick} \eta_f\} \times I(t), \tag{4.4}$$

where $I(t) = U_{in}(t) \otimes G_{b.c.}(t) \otimes F(t) \otimes U_{out}(t) \otimes G_{b.c.}(t)$.

Out of this emission flux, a certain amount will be delivered to the streak camera photocathode via a series of optical components (Fig. 4.6), including the optical fiber bundle (core diameter d=500 μm, $N.A.$=0.35), the two lenses (1:1 magnification) before the streak camera slit, a number of filters, the streak camera slit, the streak camera input lens (1:3 magnification, $F\#$=2.5 in air, thus $F\#$=3.33 in water), and the slit-shaped (height H=150 μm, width W=6 mm) photocathode. This optical relay is designed so that the system throughput is only limited by the physical properties of the streak camera input optics and photocathode, which can be estimated, for each collection channel, as

$$\eta_{throughput} = \frac{\pi}{4}d^2 \frac{3H}{d} \frac{\pi(\frac{1}{2F\#})^2}{2\pi} = \frac{3\pi dH}{32(F\#)^2} = 2.0 \times 10^{-3} mm^2.$$ In addition, the signal is

further reduced by the packing ratio of the fiber bundle (0.5), the specular reflections at each glass-air interface (0.96^8=0.7), the transmission through the two Raman edge filters (0.85^2=0.7), the long pass filter (0.9), and the streak camera input optics (0.6). (i.e.,
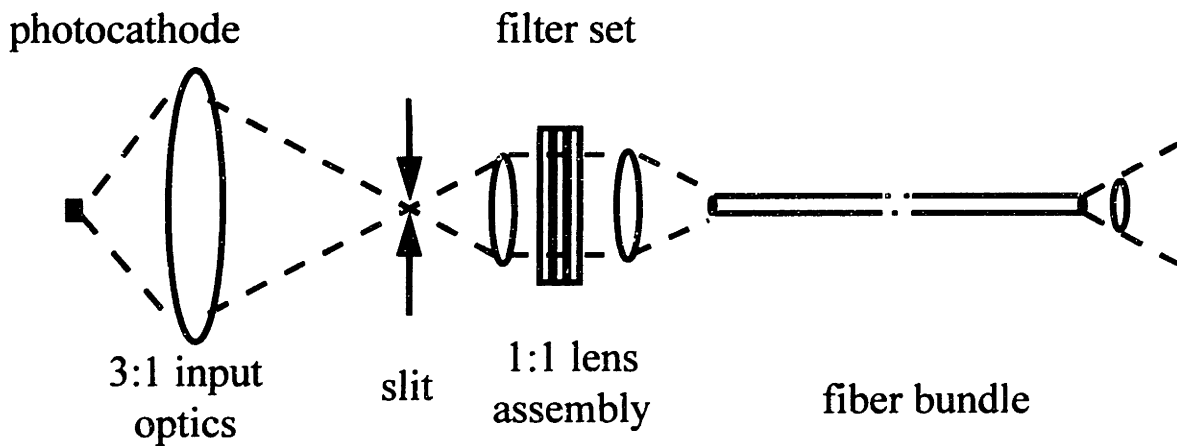
Figure 4.6. Schematic diagram of optical relay components.

$$\eta_{trans} = 0.5 \times 0.7 \times 0.7 \times 0.9 \times 0.6).$$

Within the streak camera, Fig. 4.7, several additional processes occur before the fluorescence signals are recorded by the CCD. First, after the photons hit the photocathode, a certain percentage, i.e., the photocathode quantum efficiency, $\eta_{p.c.}$, of them will generate photoelectrons (for an S-20 photocathode, $\eta_{p.c} = 3\%$ at 750-800 nm). The useful number of photoelectrons is then reduced by the acceleration mesh (0.6) and microchannel plate (MCP) packing ratio (0.5). Next, these electrons are amplified by the MCP gain, converted back to photons by the phosphor screen, and then the photons are recorded by the CCD array. As a result, with the highest MCP gain setting, which is used in all the experimental studies in this thesis, each electron entering MCP gives rise to about 18 CCD counts/pixel over about 3x3 CCD pixels. Note that each vertical CCD pixel corresponds to about 3 ps at sweep speed four. During the CCD readout (30 Hz), if the CCD is operated in the analog mode, the actual number of CCD counts plus readout

Figure 4.7. Schematic diagram of the streak camera components.

noise, roughly 6 counts/pixel, is recorded. A DC-subtraction is then needed afterward. In contrast, if the CCD is operated in the digital mode, either a 1 or a 0 is recorded for each CC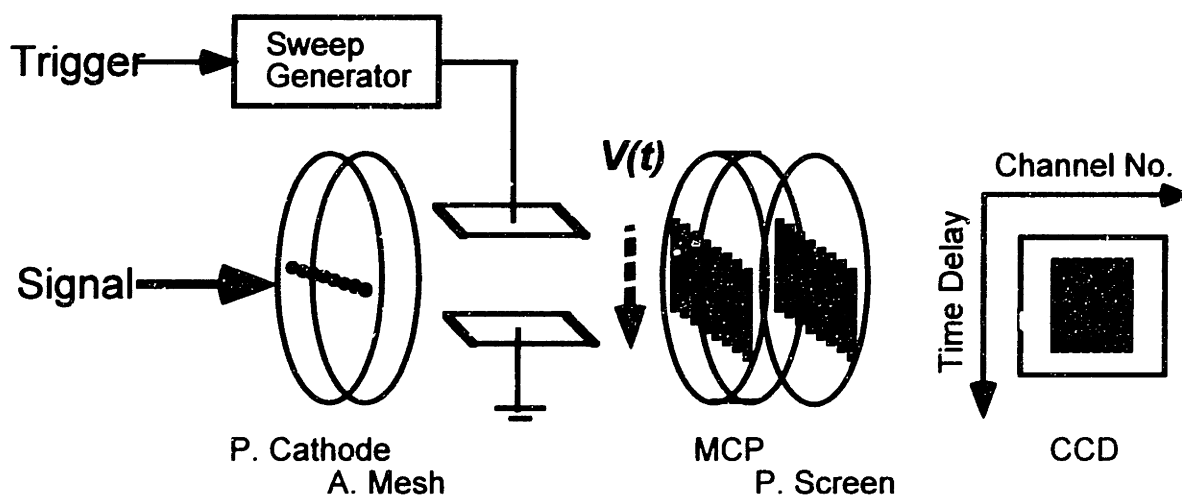D pixel, depending on whether the actual CCD count is higher or lower than the threshold value (typically set at 10 counts/pixel). This function is advantageous at low signal levels, since it removes the CCD readout noise completely. Considering all the above factors, we may write $\eta_{s.c.} = (\eta_{p.c.} \times 0.6 \times 0.5 \times 9 \times 3ps)$ for the digital mode and $\eta_{s.c.} = (\eta_{p.c.} \times 0.6 \times 0.5 \times 9 \times 18 \times 3ps)$ for the analog mode (sweep speed four).

In summary, the signal level, S, in terms of CCD count, in our experiments is determined by all the above factors, including the laser power, data accumulation time, photon migration in the medium, absorption and fluorescence emission, optical transmission, photon-to-electron conversion, electron transmission and amplification, electron-to-photon conversion and CCD registration and recording:

$$N\{\mu_a a^3 r_{thick} \eta_f\} \times I(t) \times \eta_{opt-elec}, \tag{4.5}$$

where $\eta_{opt-elec} = \eta_{throughput} \times \eta_{trans} \times \eta_{s.c.}$ consists of all the steps from the distal ends of the fibers to the CCD. In digital CCD mode and sweep speed four,

$\eta_{opt-elec}$
$$= \{2.0 \times 10^{-3} mm^2\} \times \{0.5 \times 0.7 \times 0.7 \times 0.9 \times 0.6\} \times \{0.03 \times 0.6 \times 0.5 \times 9 \times 3ps\} \tag{4.6}$$
$$= 6.4 \times 10^{-5} mm^2 ps.$$

A simple way to estimate the expected signal level in the experiment is to compare the peak value in the time-resolved curve, which can be obtained without evaluating the exact convolution integral in Eq. 4.5. Consider the convolution theorem using the Laplace transform (see Chapter 2), we know, if

$$A(t) = A_1(t) \otimes A_2(t),$$ (4.7.a)

then

$$\tilde{A}(s) = \tilde{A}_1(s) \times \tilde{A}_2(s).$$ (4.7.b)

where $\tilde{A}(s=0) = \int_0^{+\infty} A(t)dt$ is simply the area under the time-resolved curve $A(t)$.

Therefore, Eq. 4.7.b indicates that the area under the resulting curve is the product of the area under each individual curve to be convolved. We further approximate the "area" as the product of the peak value and the "width" of the curve, and assume

$$(width\ of\ A)^2 = (width\ of\ A_1)^2 + (width\ of\ A_2)^2.$$ (4.8)

Note that Eq. 4.8 is rigorous if all of the curves to be convolved are Gaussian. Therefore, the peak value of the resulting curve can be estimated as

$$(peak\ value\ of\ A) = (area\ of\ A_1) \times (area\ of\ A_2)\ /\ (width\ of\ A).$$ (4.9)

The "areas" and "widths" of each individual curve used in this estimation are listed in Table 4.1. By applying Eq. 4.9 to Eq. 4.5, the fluorescence signal level at the peak is estimated as

$$S_{peak} = N_0 \times \{\mu_a a^3 r_{thick} \eta_f\} \times I_{peak} \times \eta_{opt-elec}$$

$$= \{1.4 \times 10^{20}\} \times \{(1mm)^2 \times 0.14\} \times \{\frac{6.0 \times 10^{-9}\ mm^{-4}}{1200ps}\} \times \{6.4 \times 10^{-4}\ mm^2 ps\}$$ (4.10)

$$\approx 6000\ \text{CCD counts per time pixel per channel.}$$

This result is in good agreement with the experimental measurement considering numerous approximations and uncertainties involved in the rough estimation. (In fact, the peak of the signal curve is not detected in the actual experiment because it is at a later time than the time window. We here estimate that the peak value to be twice the intensity

observed in the last time pixel, i.e., ~ 2 x 3,600 CCD counts.) This agreement suggests that the experimental system is functioning properly as expected and that the simple theoretical model is appropriate in analyzing the experimental data.

	"Area"	"Width"
$U_{in}(t)$	3.9e-4 mm^{-2}	300 ps
$U_{out}(t)$	2.3e-5 mm^{-2}	750 ps
$F(t)$	1.0	900 ps
$G_{b.c.}(t)$	0.82	60 ps
$I(t)$	6.0e-9 mm^{-4}	1200 ps

Table 4.1. The "areas" and the "widths" of each individual curves to be convolved in Eq. 4.4. Note that the $G_{b.c.}(t)$ term is used twice in the calculation.

As for the noise, the major noise sources in the system are the shot noise, the photocathode dark current, and the CCD readout noise. Since the CCD readout noise can always be removed under digital-mode operation, and the photocathode dark current for an S-20 photocathode is very small (8×10^{-4} CCD counts/pixel/sec), our system is shot noise limited, and the noise (i.e., the standard deviation from the mean [Bevington, 1969]) can thus be estimated as the square root of the photoelectron count at the entrance of the microchannel plate. As explained earlier, this count can be estimated as (CCD counts)/(9x18) in the analog mode or (CCD counts)/9 in the digital mode. As expected, this is also in good agreement with that observed in the experiment. For example, at ~ 2400 CCD counts, the noise level is ~ 90 CCD counts in the measurement; whereas the

77

estimation gives $\sqrt{2400/9} \times 9 / \sqrt{3} = 85$ CCD counts, where $\sqrt{3}$ is due to the correlation between adjacent temporal pixels (3x3 spread on the CCD).

4.3 Inverse Tomographic Algorithm

In the previous Section, the preliminary data showed that the prototype tomographic system is able to detect early arriving fluorescence photons to image the embedded fluorescent object. However, accurate extraction of the spatial information requires applying a theoretical model in an inverse manner. Such a model should take into account the photon migration terms of both excitation and emission photons and the fluorescence decay term. Assuming the fluorescent object to be a point source, which is appropriate in a multi-focal problem such as breast tumor screening, the observed signal is the convolution of the five terms mentioned in Section 4.2 (for simplicity, we here focus on the convolution integral but not the overall numerical constant.),

$$I(t,\vec{r}_f,\vec{r}_d) = U_{in}(t,\vec{r}_f) \otimes G_{b.c.}(t) \otimes F(t) \otimes U_{out}(t,\vec{r}_f,\vec{r}_d) \otimes G_{b.c.}(t), \tag{4.11}$$

where $\vec{r}_f$ and $\vec{r}_d$ are the positions of the embedded object and the detection fiber. Again considering the convolution theorem, Eq. (4.11) can be analyzed using the Laplace transform:

$$\tilde{I}(s,\vec{r}_f,\vec{r}_d) = \tilde{U}_{in}(s,\vec{r}_f) \bullet \tilde{G}_{b.c.}(s) \bullet \tilde{F}(s) \bullet \tilde{U}_{out}(s,\vec{r}_f,\vec{r}_d) \bullet \tilde{G}_{b.c.}(s). \tag{4.12}$$

By taking the ratio between two detection channels (1 and 2), we obtain:

$$\frac{\tilde{I}_1(s)}{\tilde{I}_2(s)} = \frac{\tilde{I}(s,\vec{r}_f,\vec{r}_1)}{\tilde{I}(s,\vec{r}_f,\vec{r}_2)} = \frac{\tilde{U}_{out}(s,\vec{r}_f,\vec{r}_1)}{\tilde{U}_{out}(s,\vec{r}_f,\vec{r}_2)}, \tag{4.13}$$

78

where $\bar{r}_1$ and $\bar{r}_2$ are the positions of the two detection fibers. Since the photon migration processes of the excitation photons and the fluorescence decay time as well as the boundary condition terms are common for all of the collection channels, four terms, U_{in}, F, and two $G_{b.c.}$'s, cancel in the Laplace ratio method, Eq. (4.13). In addition, the Laplace transformation naturally introduces a weighing factor, $\exp(-st)$, which emphasizes the early part of the signal. As mentioned before, this is advantageous in extracting accurate spatial information by using the early arriving part of the signal. Considering that the diameter of the beaker is about 1000 scattering mean free paths and that the fluorescent source is not close to the boundary, we can safely use the diffusion equation solution in an infinite medium (this can be used although the beaker is more like a semi-infinite medium because of the convolution nature of the boundary effects discussed in Chapter 2) for the photon migration curve (assuming the speed of light is 1), i.e.,

$$U(t) = \left(\frac{3\mu_s{}'}{4\pi t}\right)^{3/2} \exp(-\frac{3\mu_s{}' R^2}{4t} - \mu_a t),$$

(4.14)

Eq. (4.13) can be further simplified to [Prudnikov et al, 1986]

$$\frac{\tilde{I}_1(s)}{\tilde{I}_2(s)} = \frac{R_2}{R_1} \exp\{q(R_2 - R_1)\},$$

(4.15)

where $R_{1,2} = |\bar{r}_{1,2} - \bar{r}_f|$, and $q = \sqrt{3\mu_s{}'(\mu_a + s)}$. Equation (4.15) can be easily inverted to determine the position of the embedded object. Note that the simplicity of Eq. 4.15 is mainly due to the cancellation of the common terms in the Laplace transform space. Therefore, even in certain situations, such as small source-detector separation, where diffusion approximation is not appropriate, the Laplace transform method is still very

useful when incorporated into other theoretical methods, such as the path integral approach.

Generally speaking, Eq. (4.15) can be evaluated for a wide range of values of s. As implied earlier, different s values emphasize different parts of the time-resolved curve. Thus, the analyses at different values of s possess different capabilities for extracting spatial information. This is demonstrated in Fig. 4.8. Here we plot the time-resolved fluorescence signal, $I(t)$, calculated numerically using Eq. 4.5, with the fluorescent object at the center of the beaker. Also plotted is the curve $I(t)\exp(-st)$ with s equal to 4 ns^{-1}. It can be easily understood that the optimal s value is such that $I(t)\exp(-st)$ reaches a maximum at time t_0 which is the earliest time in the $I(t)$ curve with adequate S/N, and thus provides the best trade-off between signal size and spatial resolution. In addition, due to experimental limitations, only a narrow range of values of s can be used. On the one hand, the noise level and the limited dynamic range of the detector strongly affect the very early part of the curves, $t<t_1$, where the signal is small. Thus, s has to be smaller than some critical value, s_1, to avoid introducing a large error in the Laplace transform integration. On the other hand, because of the limited window size of the streak camera, ~ 1.5 ns, the later part of the curve, $t>t_2$, is truncated. As a result, s has to be greater than a second critical value, s_2. This leads to a second criterion for choosing the optimal s value, i.e., $\int_{t_1}^{t_2} I(t)\exp(-st)dt \approx \int_0^{+\infty} I(t)\exp(-st)dt$. Following these criteria, we can determine the optimal s value based on the S/N in phantom experiments. (Later in Section 4.5, we will show the effects of different s values on the localization accuracy.)
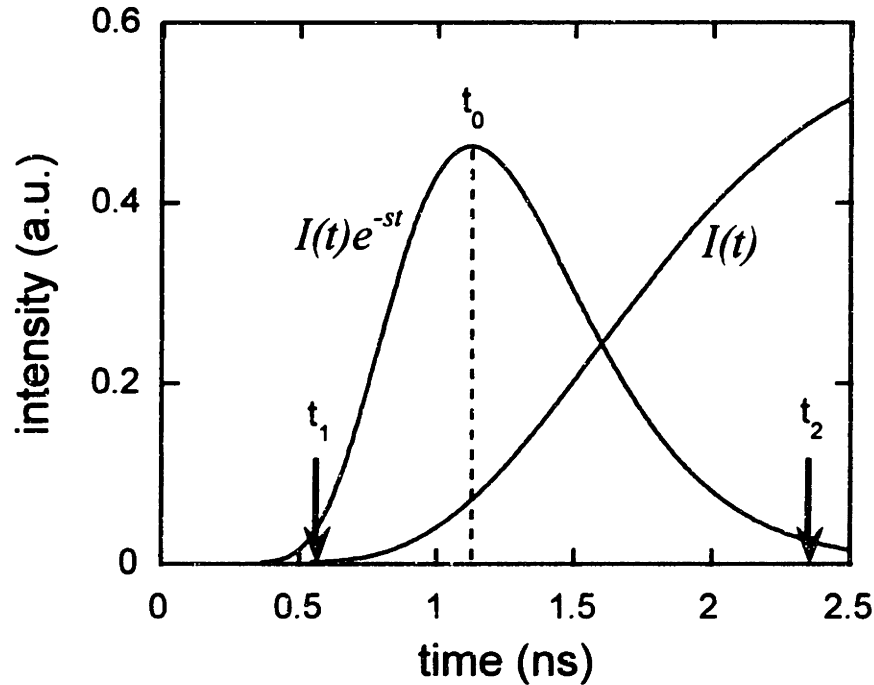
Figure 4.8. Determination of the optimal s value, based on a diffusion theory calculation. (The scales of the two curves along the y-axis are not the same.)

We can then Laplace transform the eight-channel data at the optimal s value, from which the position of the fluorescent object can be tomographically determined using Eq. (4.15).

It should be noted that the Laplace transform analysis using either a single value of s or a range of s values offer different advantages. In the cases where the tissue parameters are not known, one can obtain spatial information by fitting to Eq. (4.15) using a range of s values, with the tissue optical properties as fitting parameters. Because of the simple analytical form of Eq. (4.15), such fitting is not computationally intensive. This should be extremely useful in compensating for patient-to-patient variations in clinical applications.

On the other hand, when the tissue optical parameters are roughly known, the

analysis using a single s value is much more convenient. Thus Eq. (4.12) becomes:

$$\tilde{I}(s,\vec{r}_f,\vec{r}_d) = Q(s) \bullet \frac{1}{R_f}\exp(-qR_f)$$

(4.16)

where $R_f = |\vec{r}_d - \vec{r}_f|$, $q = \sqrt{3\mu_s'(\mu_a + s)}$ and $Q(s)$ is a numerical constant independent of

the positions of the detection channels. Without taking the ratio, there are eight, instead

of four, pieces of information available to extract the fluorophore position. The

usefulness of this simplification is better seen for the case in which two embedded objects

(a & b) are present. Here Eq. (4.16) can be modified as:

$$\tilde{I}(s,\vec{r}_f,\vec{r}_d) = Q_a(s) \bullet \frac{1}{R_a}\exp(-qR_a) + Q_b(s) \bullet \frac{1}{R_b}\exp(-qR_b)$$

(4.17)

where $R_{a,b} = |\vec{r}_d - \vec{r}_{a,b}|$. Note the number of pieces of information, 8, available is more

than the number of unknowns, 6, in this problems.

In summary, the Laplace transform allows us to extract the spatial information in a

very simple manner due to the cancellation of the common terms among the eight

detection channels. In addition, as discussed in Chapter 2, the boundary condition effects

also cancel in this analysis. Moreover, the Laplace transformation naturally introduces a

favorable weighing factor, so that the best trade-off between signal level and spatial

resolution can be achieved. O'Leary *et al* [O'Leary *et al*, 1994] reported a frequency

domain experiment (at 50 and 200 MHz) to localize a fluorophore embedded in a turbid

medium. This is mathematically equivalent to taking the Fourier transform of the time

domain signals. There is a strong mathematical similarity between the Laplace and the

Fourier transforms, and as the Fourier transform also obeys the convolution theorem, an equation similar to Eq. (4.15) could also be used, thus offering the advantage of simplification through the canceling factors. However, in this thesis study we chose the Laplace transform rather than the Fourier transform for the following reasons. (1) Physically, the Laplace transform selects a well-defined temporal window in the time domain, Fig. 4.8. In contrast, the Fourier transform selects a particular frequency component, which is not necessary localized in a given portion of the time domain signals. Thus, the Laplace transform analysis is able to emphasize the early part of the signal in a straightforward manner. (2) Our time domain data are truncated at $\sim$ 1.5 ns. Such truncation is equivalent to a temporal step function, which leads to errors in all of the frequency components. As a result, the Fourier transform of our time domain data exhibits strong oscillation as a function of frequency, due to the nature of the Fourier transform operation. On the other hand, as discussed above, the truncation error can be minimized in the Laplace transform analysis for s values of interest, i.e., those which tend to emphasize the very early part of the time-resolved signals.

4.4 Localizing and Resolving Embedded Fluorophores

Experiments were performed to study the localization and resolution performance of the prototype tomographic system using the apparatus and phantom samples detailed in Section 4.1. The embedded fluorescent objects were two 1 mm diameter glass cells filled with HITCI dissolved in methanol at 65 μM concentration. The experimental procedure was the following: (1) One fluorescent object was initially positioned at the center of the

83

beaker. It was then displaced towards Fiber Two in 1 mm steps along the direction

$\theta = \frac{\pi}{2}$, (The angle is defined in such a way that the angle for the channel i, $\theta_i = i\frac{\pi}{4}$.)

until it was 5 mm away from the center. (2) At this time, a second object was added to the

system. The second object was 5 mm from the center in the direction $\theta = \frac{5\pi}{4}$. Then the

first fluorophore was moved back towards the center again at 1 mm steps while the

second was fixed. (3) Once the first object was moved back to the center, the second

fluorophore was move towards the center by 2.5 mm. Then again the second fluorophore

was fixed and the first was moved outwards. (4) Finally, the first fluorophore was taken

out and the second was moved from the center outwards at 2.5 mm steps. Here, the

objects were always positioned in the plane of the collection fibers. However, it should

be noted that similar 3-D experiments and analysis can be done. At each object position

combination time-resolved fluorescence data was collected. The data accumulation time

was 1 minute.

From the measured curves, the Laplace transforms for eight channels were

calculated. In order to extract the spatial information, the two-object tomographic

algorithm, Eq. 4.17, was used. The s value was chosen to be 6 ns^{-1} so that a good trade-

off between the S/N and the temporal resolution (roughly $1/s$) was obtained. Here the

fitting code always assumes two objects present and predicts either two objects at two

different locations or two objects collapsed at the same location, namely, the

concentration for the second objects is close to zero. The fitting results for the above

experimental procedures (1) through (4) are shown in Figs. 4.9(a) through (d). Also

shown in Fig. 4.9 are the actual positions of the fluorescent objects. Here all the circles (triangles) are for the object 1 (2), and all the open (solid) symbols are for the actual (estimated) positions. In Fig. 4.9(a), the fitting code correctly predicts only one object present, and the average error is about 0.3 mm between the experimental estimations and the actual object positions. Similarly, in Fig. 4.9(b), the locations of both objects are correctly predicted. However, in Fig. 4.9(c), at the first three positions, the fitting algorithm predicts only one object present with its position (denoted by star) close to the "center of gravity" of the two fluorophores. In other words, the system could not resolve the two. However, as the two objects were moved further away from each other, the fitting code was able to predict the positions of both fluorophores. Not surprisingly, in Fig 4.9(d), the experimental estimation is again about 0.3 mm from the actual position. In summary, at the current S/N level, we can localize the objects with an error about 0.3 mm and we can resolve two objects if they are more than 4-5 mm apart.

At this point it is worth examining the localization results for different values of s. As compared with Fig. 4.9.a, which uses the optimal s value s=6 ns^{-1}, Fig. 4.10 plots the localization results using the same time-resolved data but with different values of s, i.e., 2 and 12 ns^{-1} in Figs. 4.10(a) and (b), respectively. In Fig. 4.10(a), the prediction is systematically further from the center than the actual positions. On the other hand, in Fig. 4.10(b), we see a random error as well as "ghost" fluorophores (denoted by stars). As explained in Section 4.3, when a too small an s is used, the truncation in the time domain introduces a systematic error in localization, whereas when too large an s is used, the noise at the very early time gets amplified, which leads to random error in the prediction.
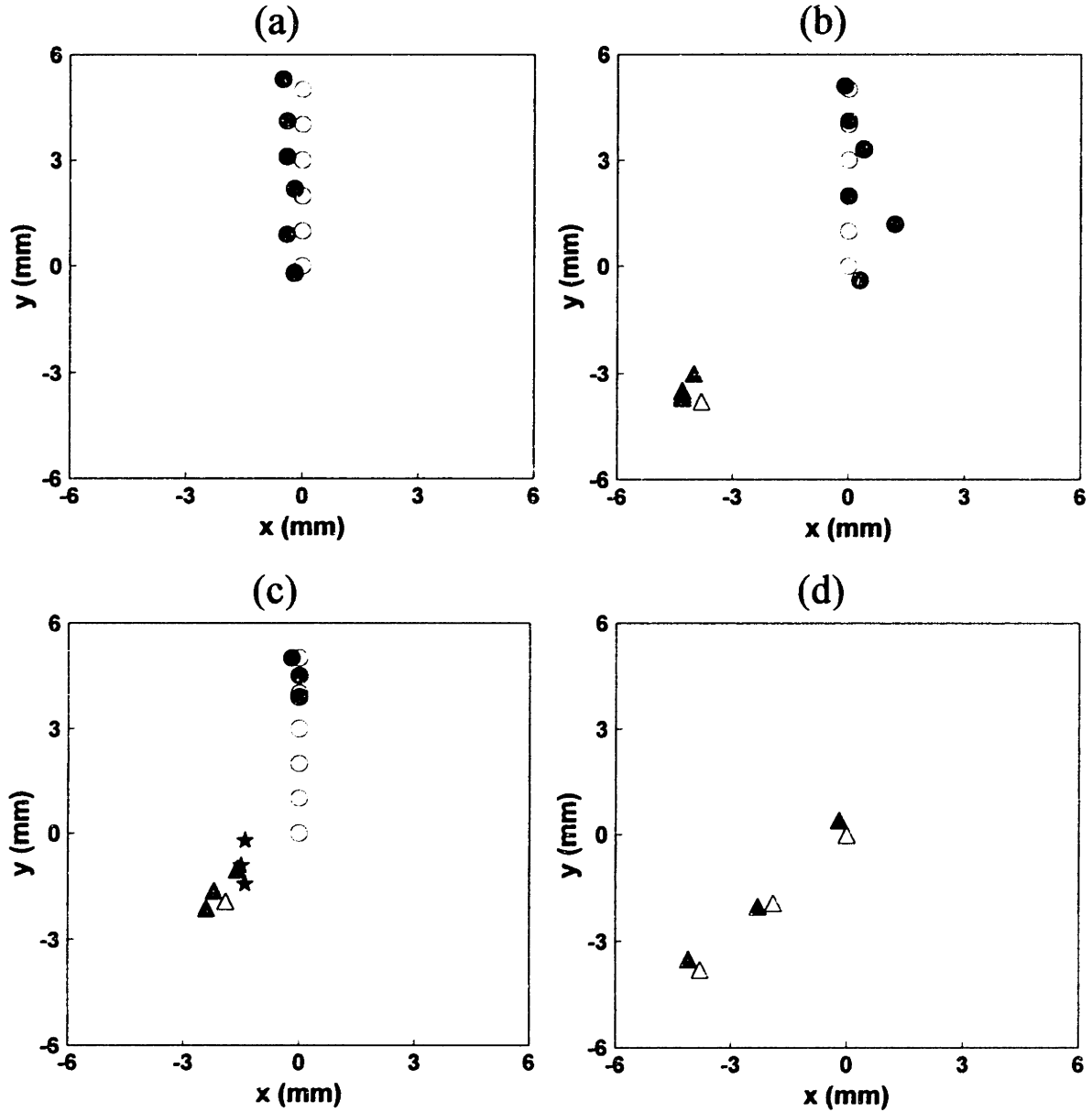
Figure 4.9. Comparison of experimentally estimated object positions to the actual positions. The open symbols are the actual positions of the objects, and the filled symbols are the experimental estimations. The stars denote the collapsed positions when the algorithm cannot resolve the two objects.
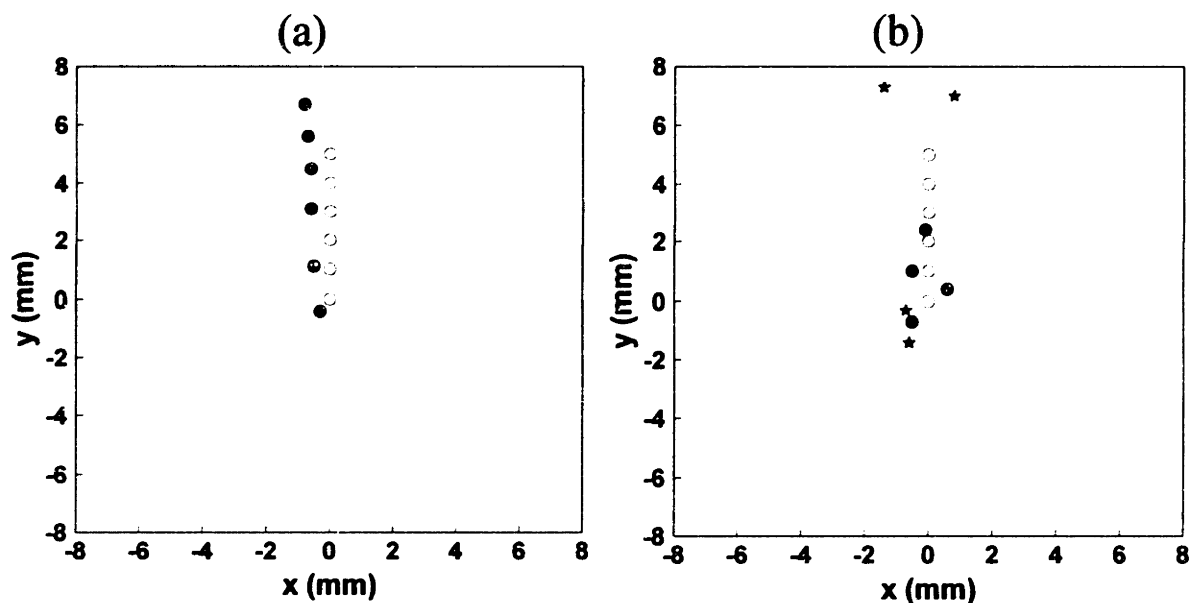
Figure 4.10. Localization results using different s values. (a) $s=2$ ns^{-1}, (b) $s=12$ ns^{-1}. The open symbols are the actual positions of the objects, and the filled symbols are the experimental estimations. The stars denote the positions of the "ghost" fluorophores.

4.5 Background Fluorescence

So far we have only considered the case in which all of the fluorescence arises from the embedded objects. However, in practical applications there are fluorescence signals from the surrounding medium as well. In fact, the observed signal level of this background fluorescence can be hundreds times larger than the signal level from the embedded objects. This is because, although the fluorophore concentration inside the embedded objects can be many times higher than the surroundings (by the factor of the contrast ratio), the volume of the medium can easily be thousands times that of the objects. Thus, any small amount of fluorophore in the surroundings can have a tremendous impact on the data analysis.

Generally speaking, this background fluorescence can be approached as two sub-problems. The first part of the problem is how to subtract this background signal. In principle, this can be done if there is an accurate theoretical model available. However, because the diffusion approximation is not correct for the case in which the fluorescence emission source is very close to the detector and/or the boundary, the theoretical modeling for the background can be extremely difficult. Experimentally, several scenarios can be proposed to subtract the background. One is to rely on a symmetric laser source-detector geometry and a uniform background fluorophore distribution, so that the background signals are identical among all the detection channels, thus will cancel after subtraction of one channel from the other. However, this approach may not be practically possible. A more practical approach is to introduce a second fluorescence agent which shows no selective accumulation inside the target, so that the background fluorescence can be measured from this reference. Moreover, considering that the selective accumulation of the contrast agent inside the tumor may take a while to happen, the background subtraction can be done by two measurements at different times, depending the pharmacodynamics/pharmacokinetics of the contrast agent.

The second part of the problem is how the noise associated with the background fluorescence signal affects the actual signal from the embedded objects, provided the background signal can be subtracted one way or the other. To address this latter point, we performed an experiment using the apparatus and phantom medium described above. A single, 5 mm diameter glass cell containing 0.65 µM HITCI was placed inside the beaker, and more HITCI was added to the medium so that the concentration in the background

was 0.065 μM (10:1 contrast ratio). The volume of the dye cell was 0.15 ml, whereas the volume of the scattering medium was 150 ml. Therefore, there was roughly 100 times more fluorophore in the background than inside the object. To remove the background signal, the fluorescence emission was collected with or without the embedded object present, and subtraction was then performed between the two to yield the signal from the embedded object plus any background noise (actually the noise is magnified by a factor of $\sqrt{2}$ by the subtraction procedure). The object was moved inside the medium at 3 mm steps, and at each position, the fluorescence signals were collected. The laser power was 100 mW and the data collection time was 1 minute. In these experiments the background signal was observed to be about 50 times stronger than the object signal, which roughly agrees with the estimation based on the product of the concentration and the volume of the fluorophore inside and outside the dye cell. As a result of the large background, the object signal measured was noisier than that measured in the zero background experiments.

After background subtraction, the Laplace transform-based inverse algorithm was used to extract the position of the embedded object. Because the noise level was higher here, a smaller value of s ($s = 3$ ns^{-1}) was used. The estimation result is shown in Fig. 4.11 together with the actual positions of the objects. In general, the experimental estimation was more accurate when the embedded object was further away from the center, with the error ranging from about 1 mm to about 2 mm when the object was less then 3 mm from the center, the average uncertainty was about 1.5 mm. This observation is understandable. When the object is off the center, certain channels are closer to the

object and receive higher signal levels, thus less sensitive to the noise level. In the meantime, signals in these channels weigh more in determining the location of the fluorophore by fitting techniques.
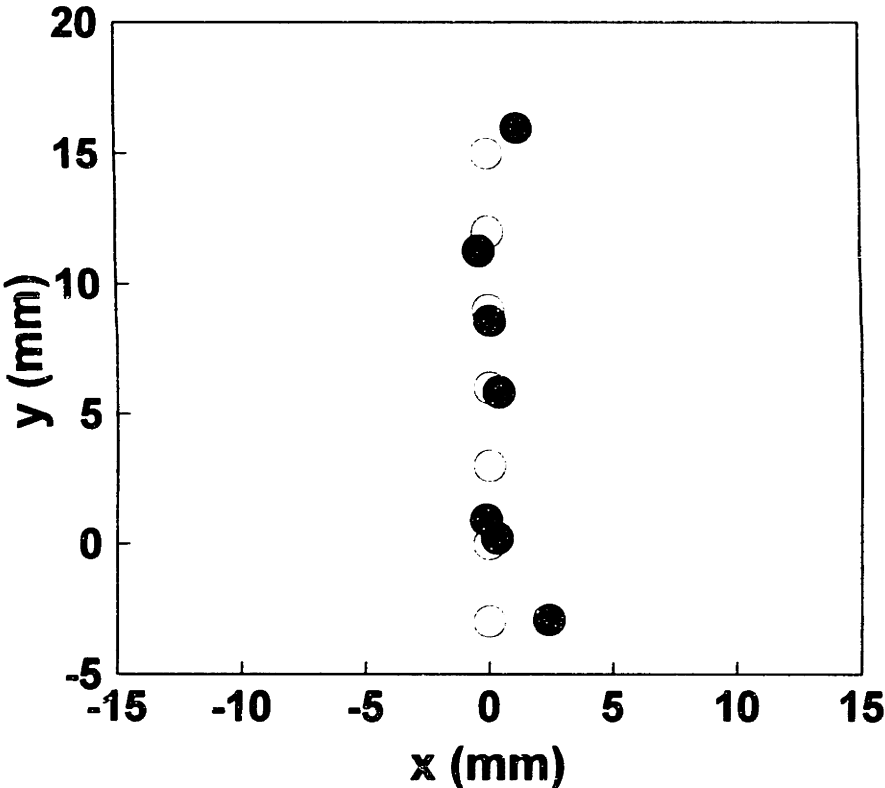
Figure 4.11. Localization result at 10:1 contrast ratio. The open symbols are the actual positions of the objects, and the filled symbols are the experimental estimations.

4.6 Algorithm accuracy

In Section 4.2, the time-domain signal and noise analysis was presented, which was shown in good agreement with that measured experimentally by the prototype tomographic system. In this section, we present an analysis that relates the localization uncertainty with the S/N in both time domain and the Laplace transformed domain.

Simply speaking, in the time domain the signal from the embedded object, S_o, is proportional to its size, a^3, the fluorophore concentration, C_o, and the absorbance of the molecule, ε, and the fluorescence quantum efficiency, η_f (assuming the object is not optical dense), as well as the laser power, P, the accumulation time, T, and the optical transmission efficiency, η_{opt} (including the photocathode quantum yield, $\eta_{p.c.}$), i.e.:

$$S = S_o \propto PTa^3 \varepsilon C_o \eta_f \eta_{opt} \qquad (4.18)$$

On the other hand, the system is shot noise limited, so that the noise term is solely determined by the total signal measured by the system. In a realistic clinical system, the background signal is usually much bigger than the object signal, so that the noise term in a single time pixel can be approximated as the square root of the number of the photon counts of the background signal, S_b. Similar to S_o, S_b can be estimated to be proportional to the fluorophore concentration within the surroundings, C_b, as well as η_f, ε, P, T, and η_{opt}. Thus the noise term is given by:

$$N = \sqrt{S_b} \propto \sqrt{PT\varepsilon C_b \eta_f \eta_{opt}} \qquad (4.19)$$

Note this analysis assumes a constant background volume. In principle, the volume factor can also be included in the S/N analysis. However, its major effect is on the photon migration terms, U_{in} and U_{out}, rather than as a simple proportionality constant.

Therefore, the S/N of the system is given by:

$$S / N \propto \sqrt{PT\varepsilon C_o \frac{C_o}{C_b} \eta_f \eta_{opt}} a^3 = \sqrt{\Sigma} a^3 \qquad (4.20)$$

where $\dfrac{C_o}{C_b}$ is the contrast ratio, and all the factors under the square root can be lumped together into a single parameter, Σ. Note that perfect background signal subtraction is assumed here.

The S/N in the Laplace transformation can be similarly described by Eq. (4.20). Note, however, the proportionality constant is a function of the value of s. Here, the absolute S/N in Laplace transform space can be estimated based on the absolute S/N in the time-resolved data, as the following. In Laplace transform space, the signal from the embedded object is just the Laplace transformation integral of the time-resolved signal, S_o, i.e.,

$$S = \widetilde{S}_o(s) \tag{4.21}$$

On the other hand, the noise can be estimated from the noise level at each time pixel as:

$$N = \sqrt{\sum_i [N(t_i)\exp(-st_i)]^2} = \sqrt{\sum_i S_b(t_i)\exp(-2st_i)} = \sqrt{\widetilde{S}_b(2s)} \tag{4.22}$$

with $\sum\limits_i$ summing over all the time pixels (i.e., Laplace transform integral over discrete data points). Thus, the absolute S/N level in the Laplace transform space can be easily evaluated from the time-resolved signals, S_o and S_b, in terms of actual photon counts.

The next step is to determine the relationship between the S/N and the localization uncertainty using the Laplace transform-based tomographic algorithm. This can be done by either computer simulations or actual experiments. In the computer simulation method, the expected signal from an embedded object was first calculated for all the eight collection channels using:

$$S_o = \frac{1}{4\pi Dr} \exp(-\sqrt{3\mu_s'(\mu_a + s)} r) \qquad (4.23)$$

where r is the distance between the fluorescent object and a given detection fiber. The same s value, $s = 3$ ns^{-1}, as in Section 4.4 was used. For simplicity, it was assumed the object is displaced from the center in the direction of a given collection channel, say channel two, by a certain distance. All the expected signals were normalized to the signal level in the case where the object is at the center. Then, Gaussian distributed noise was added to the calculated signals of every channels. Again, the noise level was normalized to the signal level from the object at the center. Finally, the inverse algorithm was applied to the sum of the calculated signals and the added noises from all the eight
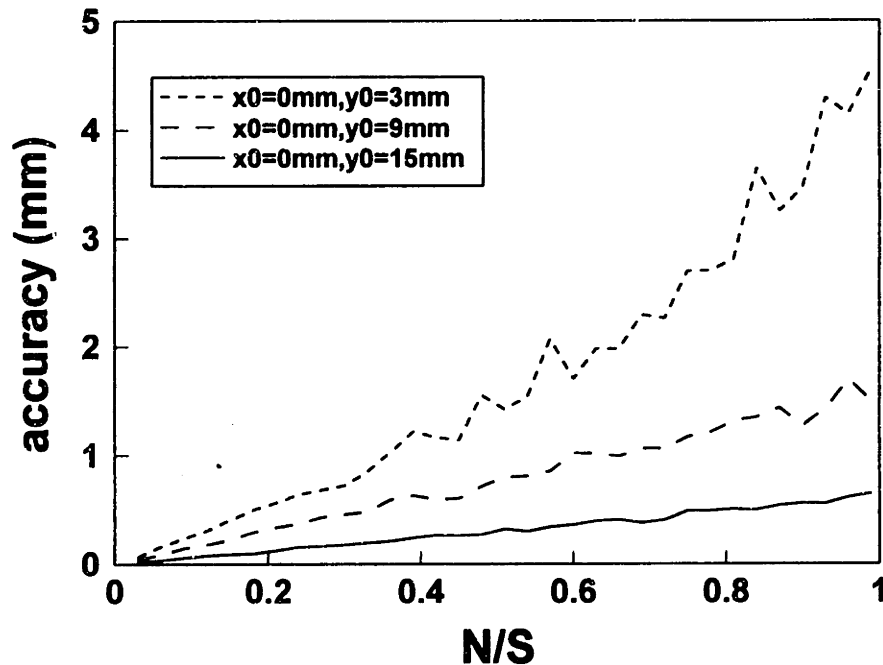

Figure 4.12 Computer simulation result (s=3 ns^{-1}) of the relationship between signal-to-noise level and the algorithm accuracy. x_0 and y_0 define the actual position of the embedded object.

channels to extract the spatial location of the object. Typically, sixty-four calculations were performed for a given set of parameters by using a different random number generator seed to generate each noise sequence. The localization uncertainty was then estimated as the average error between the actual positions and the predicted positions from the sixty-four calculations. Generally speaking, this uncertainty is a function of the noise level, as well as the actual position of the object from the center of the beaker. For the reasons indicated in Section 4.5, it is expected the error is largest when the object is right at the center. Figure 4.12 shows the average localization error as a function of the noise level and the actual position of the object (3, 9, 15 mm from the center). As expected, the prediction error is larger for the higher noise level and near-center object position, which was observed in the experimental data shown in Section 4.5. Interestingly, the prediction error is roughly proportional to the noise level for a wide range of S/N, even though the inverse model is not a linear model at all.

The relationship between the S/N and the localization uncertainty can also be evaluated experimentally. The phantom experiments were performed using the experimental parameters described in the Section 4.5, except that the data accumulation time was 6 seconds, instead of 1 minute, and the fluorophore concentration within the object was 2 μM. Since the background fluorophore concentration was kept the same, the contrast ratio was 30:1. Note the parameter, Σ, was kept roughly constant, thus the S/N in these experiments was about the same as that in the experiments described in the Section 4.5. The object was positioned at 3 mm from the center of the beaker. The time-resolved signals were repetitively measured with and without the embedded object present. A total

of twenty seven sets of data were obtained. For each single set background subtraction was performed, and then the location of the object was estimated using the inverse algorithm and compared to the actual position. The average localization uncertainty was further determined by averaging the error in all of the data sets. The twenty seven sets were then separated into nine groups, and within each group, three data were added together to generate a new data with an improved S/N (by a factor of $\sqrt{3}$). Again, the average localization error was estimated at the new S/N level. Lastly, similar analysis was done by grouping nine into three sets and by grouping all the twenty seven into a single set. So far the S/N is only defined relatively. The absolute S/N in the Laplace transform space (defined as in the computer simulation procedure) can be obtained by using Eqs. 4.21 and 4.22.

In Fig. 4.13, the experimental localization uncertainty is plotted against the N/S levels. As the computer simulation suggested, a linear relationship is observed. In addition, the experimental result agrees quantitatively (within 20%) with the computer simulation, Fig. 4.12. Furthermore, this study confirms the localization results presented in Section 4.5.

Once validated by the experiments, the computer simulations can be used to study the S/N and the localization uncertainty in a broader spectrum. For example, same analysis can be done at other s values as well. Figure 4.14 plots the simulation predicted uncertainty as the function of noise level for several object locations using $s = 6$ ns^{-1}. In general, the uncertainty is decreased by using a higher value of s. This can be understood from Eq. 4.23. Note that the exponent term is always the dominant determinant, thus any
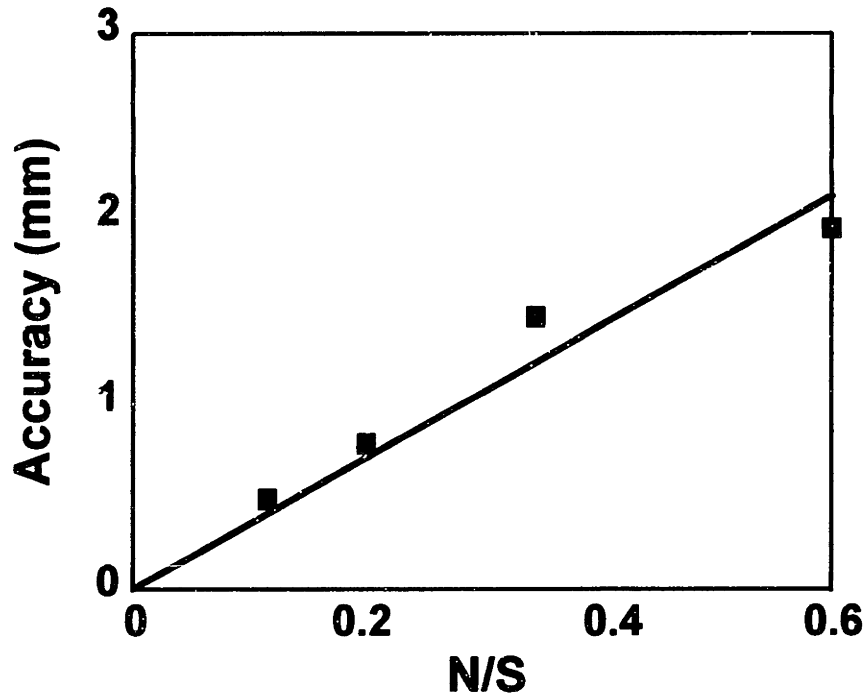
Figure. 4.13. Experimental result (s=3 ns^{-1}) of the relationship between signal-to-noise level and the algorithm accuracy.

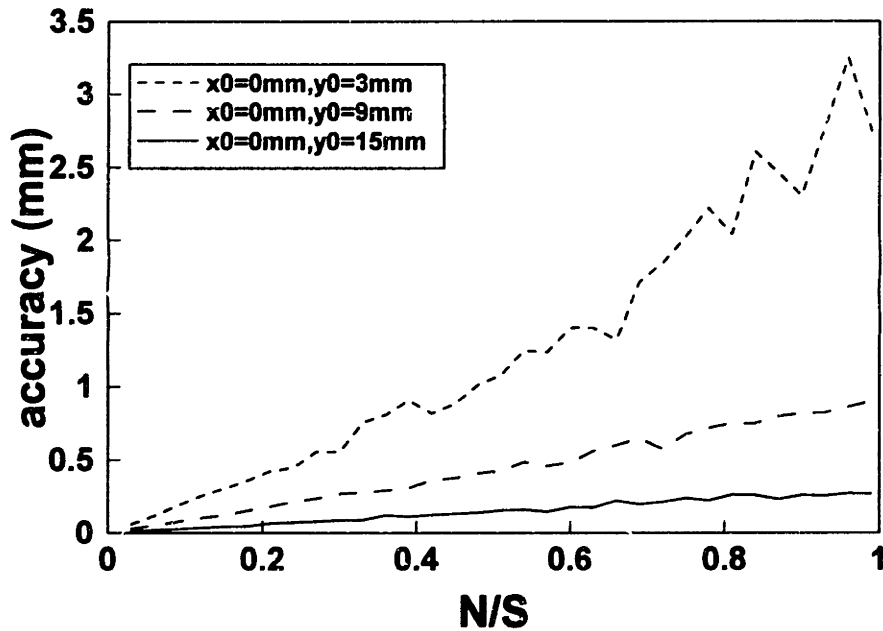Figure. 4.14 Computer simulation result (s=6 ns^{-1}) of the relationship between signal-to-noise level and the algorithm accuracy. x_0 and y_0 define the actual position of the embedded object.

spatial prediction is roughly inverse proportional to $\sqrt{3\mu_s'(s+\mu_a)}$ under a given S/N, which is in good agreement when comparing Fig. 4.12 and 4.14.

Moreover, the accuracy of the inverse algorithm critically depends on the number of detection channels. If we double the number of detection channels, the localization uncertainty can be dramatically improved, as shown in Fig. 4.15. Note this improvement is about a factor of 2 (more than $\sqrt{2}$), because the increased number of the detection channels not only increases the total S/N level in the experiment, but also provides addition information along new directions surrounding the beaker.
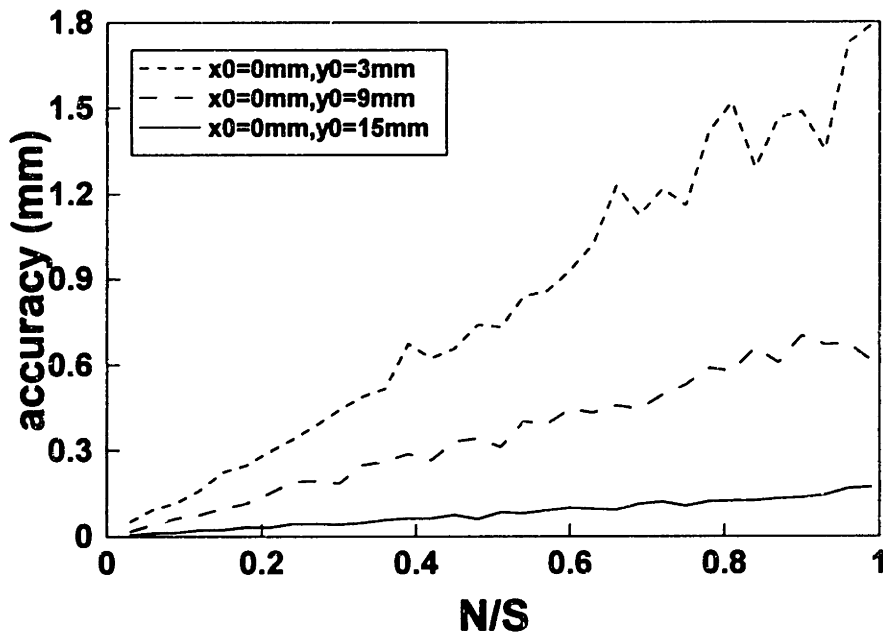

Figure 4.15. Computer simulation result ($s=3$ ns^{-1}) of the relationship between signal-to-noise level and the algorithm accuracy with 16 detection channels. x_0 and y_0 define the actual position of the embedded object.

4.7 Clinical Perspectives

Based on the above analysis, it is possible to predict the system performance for potentially relevant clinical contrast agents. By combining the S/N analysis in both time and Laplace transform domains, the linear relationship between the S/N and the localization accuracy, and the experimental result shown earlier, we obtain:

$$\sqrt{PT\varepsilon C_o \frac{C_o}{C_b} \eta_f \eta_{p.c.} a^3 \Delta} = \text{constant}, \tag{4.24}$$

where Δ is the localization uncertainty, and the constant $= 32$ $W^{1/2}sec^{1/2}mm^{7/2}$, as determined by the experimental parameters and results presented earlier. Note that in practical applications, it is desired that the localization uncertainty is about half the size of the object. In addition, the optical density of the object, i.e., $\varepsilon C_o a \ln 10$, is preferably smaller than one (i.e., not optically thick), so that a maximum amount of fluorescence signal is obtained from the same amount of fluorophore molecules.

Table 4.2 summarizes the results of analyzing the use of several clinical contrast agents in diagnosing breast tumor. (1) Various tumors express tumor-specific antigens on the cell surfaces due to the underlying genetic changes in the neoplastic process [Abbas et al, 1994]. Fluorescence-labeled anti-tumor antibodies (F-Ab's) have been suggested for tumor diagnosis [Chance, 1995]. Because antigen-antibody interaction is usually highly specific [Abbas et al, 1994], high contrast ratio can be expected. In addition, highly efficient fluorescent molecules can be used to label the antibodies [Tsien & Waggoner, 1995]. However, the number of binding sites on the cell surface is usually limited, about 10,000 on each cell [Chance, 1995]. (2) PDT agents, such as hematoporphyrin derivative

(HpD) and ALA, have been shown to selectively accumulate within the tumor cells [Johansson, 1993], presumably due to both increased vasculature and increased metabolic rate of the tumor. They are currently used in clinical trials as tumor therapeutic agents. Most porphyrin molecules, in the absence of heavy metal quenching, also fluoresce moderately [Gouterman, 1978]. Therefore, they have long been suggested as fluorescence contrast agents for tumor diagnosis as well. (3) Indocyanine green (ICG), an FDA approved contrast agent, is currently used clinically in cardiovascular imaging applications. It binds to plasma proteins in the blood stream, thus its concentration in tissue is roughly proportional to the blood vessel density. This molecule is a weak fluorophore when dissolved in human plasma. Preliminary studies have been carried out to test its potential in diagnosing embedded tumors [Zhao et al, 1995].

Finally, it is worth mentioning that the current system can be improved in various ways to optimize its performance. (1) By replacing the coherent single-mode fiber bundles (packing ratio 50%) with graded-index low-dispersion fibers [Hecht, 1990], twice as many photons will be collected by the system. (2) Currently, none of the optical surface is coated to maximize the transmission at the wavelengths of interest. In addition, the filter system removes about 40% of the fluorescence light. This is another factor of $\sqrt{3}$ that can be improved in the S/N. (3) The prototype tomographic system employs eight collection fibers, however, the width of the streak camera photocathode can easily accommodate twenty four channels. The computer simulation result suggests that this will possibly result in a factor of 3 (definitely more than $\sqrt{3}$) improvement in localization accuracy. In summary, we estimate that it is possible to improve the system performance

	Phantom	F-Ab	HpD	ICG
P (mW)	100	600	600	600
T (min)	1	1	1	1
C_o (μM)	0.65	0.05[a]	7.1[f]	0.85[f]
ε (μM^{-1}mm^{-1})	0.03	0.07[b]	0.02[g]	0.05[i]
C_o/C_b	10	50[c] (500[d])	5[h]	2[j]
η_f	0.14	0.7[b]	0.07[h]	0.0001[j]
$\eta_{p.c.}$	0.03	0.05[e]	0.05[e]	0.02[k]
a (mm)	5	2.7[c] (2.1[d])	3.1	10.2
Δ (mm)	1.5	1.4[c] (1.0[d])	1.5	5.1

[a] Assuming 10,000 antibody binding sites per cell; cell diameter 10 mm [Chance, 1995]; 50% occupancy; 5 fluorophore molecules per antibodies without significant quenching.

[b] Allophycocyanine [Tsien & Waggoner, 1995]

[c] Assuming antigen-antibody binding disassociation constant, $K_d = 10^{-9}$ μM (typically 10^{-11} μM< K_d < 10^{-7} μM [Abbas et al, 1994]); 50% binding site occupancy; 20% interstitial space in tissue. Ligand binding fraction to cell surface receptor: $f=C/(C+K_d)$ where C is the interstitial ligand concentration [Mathews & Van Holde, 1990].

[d] Assuming antigen-antibody binding disassociation constant, $K_d = 10^{-10}$ μM.

[e] Fluorescence emission wavelength 650-700 nm.

[f] Optimized so that $C_o \varepsilon a ln 10 = 1$.

[g] Porphyrin Q band [Gouterman, 1978].

[h] Estimated.

[i] Measured using Shimadzu UV-265 spectrophotometer.

[j] Private communication with Dr. Chance.

[k] Fluorescence emission wavelength 800-850 nm.

Table 4.2. Clinical perspectives of using various contrast agents.

further so that it can localize the embedded object with an accuracy of 5-7 times better or it can detect an object 40-50% smaller than the above analysis.

4.8 Conclusions

This chapter presents a prototype tomographic system consisting a picosecond pulsed laser system and streak camera. This system is able to provide high temporal resolution, single-photon-counting capability, and multichannel detection. A simple tomographic algorithm using the Laplace transformation is developed. In addition, the S/N of the system is estimated in both time and Laplace domain, which shows good agreement with the experimental measurements. Finally, a linear relationship between the S/N and the algorithm accuracy is determined from both computer simulations and experimental data.

Currently, the positions of the fluorescence objects can be localized with an uncertainty of 0.3 mm, and multiple objects can be resolved provided that that are separated by more than 4-5 mm. In practical applications, the noise associated with the background signal may have a big impact on the information extraction. With a 10:1 contrast ratio, we are currently able to locate an embedded fluorophore with an uncertainty of 1.5 mm. Lastly, by understanding the S/N and localization uncertainty of the system, we further determine the potential of this technique in clinically relevant situations, such as using fluorescence-labeled antibodies against tumor-specific antigens and PDT agents as well as ICG to detect embedded tumor. These results clearly demonstrate the feasibility of using early arriving photons to detect fluorescent objects

embedded in a turbid medium and its potential in various clinical applications, such as breast tumor screening.

When compared to other experimental approaches of photon migration imaging, our technique is unique in several aspects: (1) Unlike most works exploring either the ballistic regime or the diffusion regime, we choose the intermediate regime, i.e., the early arriving regime, to achieve the best trade-off between the S/N and the spatial resolution. (2) Instead of absorption and scattering, we use fluorescence to provide contrast. We believe that this is more clinically relevant, since various intrinsic and exogenous fluorophores have been suggested to provide diagnostic information. (3) Most studies exploring the early arriving regime do not involve the use of a theoretical model to extract the spatial information, rather, shadow images are usually constructed from the raw data [Benaron & Stevenson, 1993; Mitic *et al*, 1994]. In our approach, the Laplace transform based inverse algorithm allows us to extract the spatial information in a more systematic and more efficient manner, so that better localization accuracy and enhanced resolution can be achieved.

To our best knowledge, the result presented in this thesis is among the best ever achieved experimentally by using time-resolved imaging techniques in a phantom sample of typical tissue optical parameters and physical dimensions of human breast, at a clinically meaningful contrast ratio between the embedded inhomogeneities and the surroundings. For comparison, by using diffusive photons, Jiang *et al* [Jiang *et al*, 1996] reported an image reconstruction of two embedded objects (15 mm and 8 mm in diameter, separated by 50 mm, 4:1 contrast ratio in either absorption or scattering

coefficients) in an 86 mm diameter phantom using frequency-domain (150 MHz) diffuse reflectance measurement; Boas *et al* [Boas *et al*, 1996] investigated the limits for the detection of absorption inhomogeneities using diffusing photons as a probe, and concluded that, in model breast systems with realistic S/N, a 3 mm tumor can be detected at contrast ratio of 3:1; O'Leary *et al* [O'Leary *et al*, 1994], using 50-200 MHz frequency modulation, was able to localize a 1 cm fluorescent object, without background fluorescence, with an accuracy of 4 mm in a 7 cm tissue-like phantom. By using early arriving transmitted signal, Mitic *et al* [Mitic *et al*, 1994] were able to detect perfect absorbers embedded in a 4 cm thick tissue-like phantom with a spatial resolution about 5 mm.

References

D. Benaron & D. Stevenson, 1993, "Optical time-of-flight and absorbance imaging of biologic media," Science, pp 1463.

P. Bevington, 1969, <u>Data Reduction and Error Analysis for the Physical Sciences</u>, (McGraw-Hill Book Company, New York).

D. Boas, M. O'Leary, B. Chance, & A. Yodh, 1996, "Detection and characterization of optical inhomogeneities with diffuse photon density waves: a signal-to-noise analysis," J. Opt. Soc. Am. A, submitted.

C. Bohren & D. Huffman, 1983, <u>Absorption and Scattering of Light by Small Particles</u>, (Wily, New York).

M. Gouterman, 1978, <u>Porphyrin</u>, Vol. III, Ch. 1, (Academic Press, New York).

E. Hecht, 1990, <u>Optics</u>, (Addison-Wesley Publishing Company, Reading, MA).

H. Jiang, K. Paulsen, & U. Osterberg, 1996 "Frequency-domain optical image reconstruction: initial experimental studies on contrast and resolution limit," in *Advances in Optical Imaging and Photon Migration TOPS-96*, (OSA, Orlando).

J. Johansson, 1993, *Fluorescence Spectroscopy for Medical and Environmental Diagnostics*, Ph.D. thesis, Luanda Institute of Technology, Luanda, Sweden.

C. Mathews & K. Van Holde, 1990, <u>Biochemistry</u>, (The Benjamin/Cummings Publishing Company, Inc., Redwood City, CA).

G. Mitic, J. Kolzer, J. Otto, E. Plies, G. Solkner, & W. Zinth, 1994, "Time-gated transillumination of biological tissues and tissuelike phantoms," Appl. Opt., pp 6699.

M. O'Leary, D. Boas, B. Chance, & A. Yodh, 1994, "Reradiation and imaging of diffuse photon density waves using fluorescent inhomogeneities," J. Luminescence, pp 281.

M. Patterson, B. Chance, & B. Wilson, 1989, "Time resolved reflectance and transmittance for the noninvasive measurement of tissue optical properties," Appl. Opt., pp 2331.

A. Prudnikov, I. Brychkov, & O. Marichev, 1986, Integrals and Series, (Gordon and Breach Science Publishers, New York).

L. Sokolnikoff & R. Redheffer, 1966, Mathematics of Physics and Modern Engineering, 2nd ed., (McGraw-Hill, New York).

R. Tsien & A. Waggoner, 1995, Handbook of Biological Confocal Microscopy, 2nd ed., Chapter 16, (Plenum Press, New York).

S. Zhao, M. O'Leary, S. Nioka, & B. Chance, 1995, "Breast tumor detection using continuous wave light source," SPIE 2389, pp 809.

Chapter 5

Conclusions and Future Directions

5.1 Thesis Accomplishments

This thesis has obtained new results in several areas. It has shown that the photon migration picture can be a valuable adjunct to other standard theory, such as the diffusion approximation. As was shown, it provides new physical insight into the light scattering problems and in some situations, simple analytical solutions have been derived based on this picture. In particular relevant to optical imaging studies, the photon migration picture was applied to boundary conditions, such as the tissue-air interface that is commonly encountered in non-invasive optical imaging applications (Chapter 2). This approach was shown to provide a convenient way to remove the effects of the boundary in analyzing time-resolved signals.

In addition to providing a better theoretical understanding of the underlying physical process of photon migration in turbid media, this thesis developed an optical tomographic technique which is potentially important in diagnosing clinical problems, such as breast tumor detection. The method explores early arriving fluorescence photons to provide useful information about the embedded structures. This experimental approach was designed to provide the optimal trade-off between the S/N and the spatial resolution, and an enhanced contrast between the embedded lesions and the surroundings.

In addition, it was shown that the spatial resolution of this method is not limited by the long fluorescence lifetime (Chapter 3).

A prototype tomographic system consisting of a picosecond pulsed laser and a state-of-art streak camera was constructed to obtain multichannel fluorescence signals. A Laplace transform-based inverse algorithm was derived analytically to extract spatial information from the multichannel measurements. Preliminary experiments were conducted in phantom samples with typical optical and geometric parameters of human breast. The results shown that an embedded object can be localized with an accuracy about 0.3 mm, that multiple objects can be resolved if they are separated by more than 4-5 mm, and that, at 10:1 contrast ratio, the embedded fluorophore can be localized with an accuracy of 1.5 mm. These results are promising and demonstrate the potential of this technique to detect breast tumors at their early stage in clinical settings (Chapter 4).

5.2 Future Directions

So far, all of the experiments have employed phantom samples. Obviously, further studies must be done in living systems to help determine the good of this technique in clinical settings. This stage of research will involve the use of animal and/or human models with clinically relevant contrast agents. As briefly discussed in Chapter 4, numerous problems will emerge at this stage:

(1) It will be extremely important to design a suitable tumor model system to perform any biological studies. This can be either an animal model with chemical/radiation-induced malignancy or cancer patients undergoing photodynamic

therapy. It is important to realize that any animal model should simulate both the optical parameters of human tissue as well as the physical sizes of the human organs to be targeted in clinical applications.

(2) A clinically acceptable contrast agent must be carefully selected. The selection requirements will include the selective uptake within the target, clinical safety, proper pharmacodynamics/pharmacokinetics so that a relative high contrast can be maintained for a period of time, relative high absorption and fluorescence quantum efficiency, and optimal excitation and emission wavelengths within the NIR therapeutic window to achieve deep penetration. Currently, both PDT agents and fluorescence-linked anti-tumor antibodies have been suggested. For the PDT agents to be used, they must be chemically modified to quench the triplet state and enhance the fluorescence transition. Moreover, the clinically achievable contrast ratio must be studied in detail. On the other hand, fluorescence-labeled antibodies may provide much better contrast ratio. Although there are usually limited binding sites on the cell surface, high quantum yield fluorescence labels can be used to provide reasonable fluorescence signal level. Of course, before any clinical study can be performed, the specific tumor antigen must be identified, anti-tumor antibodies must be prepared and, most importantly, the antibody-antigen interaction must be extensively studied.

(3) It may be necessary to modify the experimental setup to provide the optimal excitation wavelength for the selected contrast agents. Most PDT agents currently under investigation have an excitation maximum between 600 to 700 nm. Similarly, high quantum yield fluorescence labels usually have an excitation maximum below 700 nm.

In either case, a mode-locked Nd:YAG laser pumped picosecond dye laser can be used to replace the argon laser pumped mode-locked Ti:sapphire laser currently being used in the phantom studies. Although the laser power may decrease by a factor of two, a higher quantum efficiency of photodetection in this wavelength range may well compensate for this loss. Moreover, the current system uses eight collection channels to demonstrate the principles. This can be increased by 3 fold in order to make the full use of the streak camera throughput. As suggested in Section 4.5, the increased number of detection channels will provide better accuracy in detecting the embedded lesions.

(4) Accurate background-subtraction schemes must be explored. Due to the tremendous volume ratio, the background fluorescence is expected to be higher, if not much higher, than the desired signal from the embedded tumors, especially small ones. Therefore, the background signal has to be accurately subtracted before the spatial information of the embedded lesions can be extracted. As detailed in Section 4.4, this can be done either by accurate theoretical modeling or by experimental methods using two spatial channels, two contrast agents, or two measurements at different times.

(5) Although the Laplace transform based inverse algorithm is simple and accurate in current studies, its limitations should not be overlooked. In particular, it does not provide shape and size information about the tumor. A more complete inverse algorithm, either based on the path integral approach or on the diffusion approximation, must be developed to provide such information.